

# The isotopic effects in the scattering and the kinetics of the atomic cascade of excited $\mu^-p$ and $\mu^-d$ atoms

V.P. Popov\* and V.N. Pomerantsev†

*Skobeltsyn Institute of Nuclear Physics, Lomonosov Moscow State University, 119234 Moscow, Russia*

(Dated: December 21, 2016)

The quantum-mechanical calculations of the differential and integrated cross sections of the elastic scattering, Stark transitions, and Coulomb de-excitation at collisions of excited  $\mu^-p$  and  $\mu^-d$  atoms with hydrogen isotope atoms in the ground state are performed. The scattering processes are treated in a unified manner in the framework of the close-coupling approach. The used basis includes both open and closed channels corresponding to all exotic atom states with principal quantum numbers from  $n = 1$  up to  $n_{\max} = 20$ . The energy shifts of  $ns$  states due to electron vacuum polarization and finite nuclear size are taken into account. The kinetics of atomic cascade of  $\mu^-p$  and  $\mu^-d$  atoms are studied in a wide range of relative target densities ( $\varphi = 10^{-8} - 1$ ) within the improved version of the extended cascade model, in which the results of the numerical quantum-mechanical calculations of the cross sections for quantum numbers and kinetic energies of muonic atoms, that are of interest for the detailed cascade calculations, are used as input data. Initial  $(n, l, E)$ -distributions of muonic atoms at the instant of their formation and the target motion are taken into account explicitly in present cascade calculations. The comparison of the calculated cross sections, the kinetic energy distributions of muonic atoms at the instant of their  $np \rightarrow 1s$  radiative transitions as well as the absolute and relative  $x$ -ray yields for both muonic hydrogen and muonic deuterium reveals the isotopic effects, which, in principal, may be observed experimentally. The present results are mainly in very good agreement with experimental data available in the literature.

PACS numbers:

## I. INTRODUCTION

The muonic and hadronic hydrogen-like atoms ( $\mu^-p$ ,  $\mu^-d$ ,  $\pi^-p$ ,  $\pi^-d$ , etc.) are formed in highly-excited states, when a heavy negatively charged particle ( $\mu^-$ ,  $\pi^-$ ,  $K^-$ , etc.) is slowed down in the gaseous or liquid hydrogen target and captured on the atomic orbit. After the exotic atom formation, its initial distributions in quantum numbers and kinetic energy are changed during the so-called atomic cascade through a number of processes: radiative and Stark transitions, elastic scattering, external Auger effect, Coulomb de-excitation (CD), weak decay, and strong absorption in the case of hadronic atoms.

The general features of these exotic atoms are similar to ones of ordinary hydrogen atoms, because their level structure is mainly determined by the static Coulomb interaction. However, due to significant differences of exotic particle and electron masses, the distance scale in the exotic atom case is much smaller, while the energy scale is much larger in comparison with the usual atomic scale. These scale effects make possible to realize the processes of external Auger effect and CD and open additional opportunities for study of the quantum electrodynamics, weak or strong interactions (in the case of hadronic atoms), and scattering processes in collisions of the exotic and ordinary hydrogen isotope atoms.

The muonic atoms of hydrogen isotopes are the simplest of exotic atoms and may be considered as ideal objects to study the isotopic effects in the lightest exotic atoms. Their experimental and theoretical investi-

gations serve as the best probe to study various collisional processes of these atoms with ordinary hydrogen isotope atoms or molecules. A good understanding of isotopic effects in the scattering and kinetics of the atomic cascade of muonic hydrogen and deuterium constitutes a very important foundation for pionic deuterium and muonic tritium predictions. Besides, they are of particular interest in order to reach the reliable theoretical description of the scattering and de-excitation cascade in the case of hadronic atoms. The last is especially important for the proper analysis of the precise spectroscopic experiments with pionic [1], kaonic [2], and antiprotonic [3] hydrogen isotope atoms, aimed at extraction of strong interaction widths of low angular-momentum states.

The experimental data, such as  $x$ -ray yields, the products of strong interaction, the shapes of  $x$ -ray lines, and the kinetic energy distribution of exotic atoms in their ground states, are mainly related to the last stage of the atomic cascade. Therefore, the study of the kinetics of atomic cascade in hydrogen media provides the only test of both theoretical approaches used to describe the collisional processes and cascade models. From the other hand, the realistic theoretical description of all processes involved in the atomic cascade plays also a key role to choose optimal experimental conditions and to improve the quality of the analysis of experimental data.

The first theoretical study of the atomic cascade in exotic hydrogen-like ( $\pi^-p$  and  $K^-p$ ) atoms has been performed by Leon and Bethe [4] more than fifty years ago. In this paper and later in more refined models [5, 6], beyond radiative transition rates, only collisional rates of the Stark mixing and external Auger effect, calculated respectively in the semiclassical and Born approximation at a fixed kinetic energy ( $\sim 1$  eV), have been taken into account to simulate the atomic cascade. In these cascade calculations the scaling factors for the Stark mixing and

\*Electronic address: popov@nucl-th.sinp.msu.ru

†Electronic address: pomeran@nucl-th.sinp.msu.ru

external Auger effect rates were used and, besides, the kinetic energy was treated as a fit parameter.

However, the high-energy fractions have been found in energy distributions of  $\mu^-p$ ,  $\mu^-d$  and  $\pi^-p$  atoms in the different time-of-flight experiments [7–10]. In particular, the high-energy components have been found in the neutron time-of-flight experiments (see [7] and references therein) with pionic hydrogen and in diffusion experiments [9, 10] with muonic hydrogen and deuterium atoms.

The extended standard cascade model (ESCM) [11, 12] introduces a number of improvements compared to the earlier models: for example, the scattering from molecular hydrogen at high  $n$  is calculated as opposed to the phenomenological treatment in other cascade models. Cascade calculations in this model include the evolution of the kinetic energy during de-excitation cascade. However, the ESCM predictions could not describe a number of experimental data, in which the kinetic energy distribution of an exotic atom at the instant of its  $x$ -ray emission from a specific level in muonic [13, 14] and pionic (e.g., see [15] and references therein) atoms or at the time of the charge-exchange reaction (neutron time-of-flight experiment [7]) is needed for the analysis of the experimental data.

To interpret and analyze these experimental data a more sophisticated approach based on the reliable and self-consistent description of all essential collisional processes involved in the de-excitation cascade is required. The processes of elastic scattering, Stark transitions, and CD appear to be of significant importance, because of their considerable influence on the kinetic energy distribution of exotic atoms during the atomic cascade.

The study of the elastic scattering and Stark mixing cross sections in the exotic atom - ordinary hydrogen atom collisions has been performed within a fully quantum-mechanical adiabatic approach [16–19] about fifteen years ago. Later, these cross sections have been also calculated in the framework of the close-coupling model [20] applying the screening dipole approximation to describe the exotic atom-hydrogen atom interaction for the low states  $n = 2 - 5$ . However, this approximation can not be justified for low-energy scattering (see [19]). Thus, the latter approach as well as various modifications of the semiclassical model [5, 6, 20] lead to unreliable results in the low-energy region where only the lowest partial waves are important.

The theoretical study of the CD has also a long history (e.g., see [21–27]). Nevertheless, in the most important region  $n = 2 - 8$  of the principal quantum number, relevant for the kinetics of the atomic cascade, this process has been regarded as the least studied until last decade [28–31].

The present research continues the cycle of our papers devoted to the detailed theoretical study of the scattering processes and the kinetics of the atomic cascade in lightest exotic hydrogen-like atoms. In particular, in our previous papers (e.g., see [28–31]), the dynamics of collisions of excited exotic atoms with hydrogen ones has been studied in the framework of the close-coupling approach.

The present study has at least three main goals. First,

to obtain in framework of a unified quantum-mechanical approach the cross sections of elastic scattering, Stark transitions, and CD in collisions of excited  $\mu^-d$  atoms with ordinary deuterium atoms, which, according to our knowledge, have never been calculated before. Second, to provide a comprehensive set of differential and integrated cross sections for all collisional transitions  $nl \rightarrow n'l'$  in  $\mu^-p$  and  $\mu^-d$  atoms at relative energies needed for the detailed study of the kinetics of the de-excitation cascade in the hydrogen isotope targets. Finally, to investigate isotopic effects in the scattering cross sections of excited  $\mu^-p$  and  $\mu^-d$  atoms, calculated on the same theoretical footing, and in various characteristics of the atomic cascade, such as absolute and relative  $x$ -ray yields, kinetic energy distributions of muonic hydrogen and deuterium atoms at the instant of their radiative transitions, and cascade times.

The paper is organized as follows. The brief description of the theoretical approach used to describe the scattering of the excited muonic hydrogen and deuterium atoms in the hydrogen isotope targets is given in Sec. II. In Sec. III, we demonstrate the typical examples illustrating the closed channel effect and the convergence of calculated cross sections relative to the extension of the basis and the number of partial waves taken into account. The isotopic effect in the scattering cross sections and rates of different CD is also represented in Sec. III. The kinetics of the atomic cascade of  $\mu^-p$  and  $\mu^-d$  atoms is studied in Sec. IV. Here, the various results calculated in the improved version of the atomic cascade are presented and compared with the known experimental data. The conclusions are summarized in Sec. V.

Atomic units are used unless otherwise stated.

## II. CROSS SECTIONS OF THE COLLISIONAL PROCESSES

### A. Main features of the approach

To study the scattering processes in collisions of  $(\mu^-p)_{nl}$  and  $(\mu^-d)_{nl}$  atoms in the excited  $(nl)$  states ( $n$  and  $l$  are the principal quantum number and orbital angular momentum of the exotic atom) with ordinary hydrogen or deuterium atoms in the ground state, the close-coupling approach is applied. In the framework of this approach the processes,

$$(\mu^-a)_{nl} + (be^-)_{1s} \rightarrow (\mu^-a)_{n'l'} + (be^-)_{1s}, \quad (1)$$

of the elastic scattering ( $n' = n, l' = l$ ), Stark transitions ( $n' = n, l' \neq l$ ), and CD ( $n' \leq n - 1$ ) are treated in a unified manner. Here,  $a = b = p$  in the case of the muonic hydrogen atom, and  $a = b = d$  in the case of the muonic deuterium atom, respectively.

The close-coupling approach was applied earlier by the authors for the fully quantum-mechanical description of the scattering processes (1) in collisions of excited exotic (muonic, pionic, kaonic, and antiprotonic) hydrogen atoms with ordinary hydrogen ones [28–31] and hydrogen molecules [32], as well as for the collision-induced absorption or annihilation in the case of hadronic atoms [33, 34].

For the benefit of the reader, the outlines of the applied close-coupling approach are briefly reminded.

In this paper, as in our previous studies, the target atom is assumed to be in its ground state during the collision. In order to properly take into account the electronic degrees of freedom in considered processes, it is necessary to consider the quantum four-body problem. However, in our case we are dealing with a collision of two neutral subsystems (atoms of the muon and ordinary hydrogen). A muonic atom can be considered as a point dipole with a small dipole moment. So, the polarization of atom in the collision leads to rapidly decreasing Van der Waals interaction  $\sim 1/R^6$ . Such an interaction can affect only elastic scattering cross section. Due to the smallness of the dipole moment this effect can not be significant. Note that even in the case of alpha decay of heavy nucleus accounting distortions of the inner electron shell (due to the interaction of electrons with the charged alpha particle) has no significant effect on the rate of the alpha decay, as shown in the papers [35, 36].

Thus, at the present stage of the study of the considered processes, we are limited to the “frozen” electron approximation. Then the four-body scattering problem under consideration is reduced to the three-body one and can be described by the wave function  $\Psi_E^{JM p}(\boldsymbol{\rho}, \mathbf{R})$  of the three-body system  $(\mu^- a)_{nl} + A$  ( $A$  denotes an ordinary hydrogen or deuterium atom). The set of Jacobi coordinates  $(\mathbf{R}, \boldsymbol{\rho})$  of the system is defined as:

$$\mathbf{R} = \mathbf{R}_A - \mathbf{R}_{\mu a}, \quad \boldsymbol{\rho} = \mathbf{r}_\mu - \mathbf{r}_a. \quad (2)$$

Here,  $\mathbf{R}_A$  and  $\mathbf{R}_{\mu a}$  are the center-of-mass radius-vectors of hydrogen and exotic atoms;  $\mathbf{r}_a$  and  $\mathbf{r}_\mu$  are radius-vectors of the nucleus  $a$  and muon in the laboratory system.

At a fixed total energy  $E$  of the system, definite quantum numbers of the total angular momentum ( $J, M$ ) and parity  $p = (-1)^{l+L}$ , the exact wave function  $\Psi_E^{JM p}(\boldsymbol{\rho}, \mathbf{R})$  satisfies the time-independent Schrödinger equation,

$$(H - E)\Psi_E^{JM p}(\boldsymbol{\rho}, \mathbf{R}) = 0. \quad (3)$$

The Hamiltonian,  $H$ , after the separation of the center-of-mass motion of the total system, can be written in terms of Jacobi coordinates (2) as

$$H = -\frac{1}{2M_r}\Delta_{\mathbf{R}} + h_\mu(\boldsymbol{\rho}) + V(\boldsymbol{\rho}, \mathbf{R}), \quad (4)$$

where  $M_r = M_{\mu a}M_t/(M_{\mu a} + M_t)$  is the reduced mass of the system with  $M_{\mu a} = m_\mu + m_a$  and  $M_t = m_e + m_b$  ( $m_a, m_b, m_\mu$ , and  $m_e$  are masses of hydrogen isotopes, muon, and electron, respectively).

The Hamiltonian  $h_\mu$  of the free exotic atom involves Coulomb interaction of the non-relativistic two-body problem as well as terms leading to the energy shift of  $ns$  states relative to the degenerate  $nl$  states ( $l \neq 0$ ) mainly account for by electron vacuum polarization and nuclear finite size effects. In the case of muonic atoms

$$\langle nlm|h_\mu|nlm\rangle = E_{nl} = -\frac{0.5m_r}{n^2} - \delta_{l0}\varepsilon_{n\geq 2}^{\text{Lamb}}, \quad (5)$$

where  $\langle \boldsymbol{\rho}|nlm\rangle = R_{nl}(\rho)Y_{lm}(\hat{\boldsymbol{\rho}})$  is the hydrogen-like wave function of muonic atom in the  $nlm$  state,

$m_r = m_\mu m_a/M_{\mu a}$  is its reduced mass, and  $\varepsilon_{n\geq 2}^{\text{Lamb}}$  is the shift of the Coulomb energy level due to electron vacuum polarization and nuclear finite size effects. In the present study we use  $\varepsilon_2^{\text{Lamb}} = 202.08$  meV and  $\varepsilon_2^{\text{Lamb}} = 203.01$  meV [37] for muonic hydrogen and muonic deuterium, respectively. For  $ns$  states with  $n \geq 3$  the energy shift due to electron vacuum polarization and nuclear finite size effects is approximately calculated according to  $\varepsilon_n^{\text{Lamb}} = \varepsilon_2^{\text{Lamb}}(2/n)^3$ .

The interaction potential  $V(\boldsymbol{\rho}, \mathbf{R})$  in (4) is obtained by averaging the sum of two-body Coulomb interactions  $V_{ij}$  ( $i = a, \mu^-$  and  $j = b, e^-$ ) between particles of colliding subsystems over the ground-state wave function of the hydrogen isotope atom (for details see Appendix A).

The wave function  $\Psi_E^{JM p}(\boldsymbol{\rho}, \mathbf{R})$  of the three-body system  $(\mu^- a)_{nl} + A$  is expanded on basis states

$$\langle \boldsymbol{\rho}, \hat{\mathbf{R}}|nl, L : JM\rangle \equiv R_{nl}(\rho)\mathcal{Y}_{lL}^{JM}(\hat{\boldsymbol{\rho}}, \hat{\mathbf{R}}), \quad (6)$$

constructed from non-relativistic hydrogen-like wave functions  $\langle \boldsymbol{\rho}|nlm\rangle$  of the muonic atom and

$$\mathcal{Y}_{lL}^{JM}(\hat{\boldsymbol{\rho}}, \hat{\mathbf{R}}) \equiv i^{l+L} \sum_{m\lambda} \langle lmL\lambda|JM\rangle Y_{lm}(\hat{\boldsymbol{\rho}})Y_{L\lambda}(\hat{\mathbf{R}}). \quad (7)$$

The substitution of the expansion for  $\Psi_E^{JM p}$ ,

$$\Psi_E^{JM p}(\boldsymbol{\rho}, \mathbf{R}) = \frac{1}{R} \sum_{nlL} G_{nlL}^{EJp}(R) \langle \boldsymbol{\rho}, \hat{\mathbf{R}}|nl, L : JM\rangle, \quad (8)$$

into the Schrödinger equation (3), leads to the set of the close-coupling second-order differential equations for the radial channel wave functions  $G_{nlL}^{EJp}(R)$ :

$$\begin{aligned} & \left( \frac{d^2}{dR^2} + k_{nl}^2 - \frac{L(L+1)}{R^2} \right) G_{nlL}^{EJp}(R) \\ &= 2M_r \sum_{n'l'L'} W_{n'l'L',nlL}^{Jp}(R) G_{n'l'L'}^{EJp}(R), \end{aligned} \quad (9)$$

where

$$k_{nl}^2 = 2M_r(E_{\text{cm}} + E_{nli} - E_{nl}) \quad (10)$$

specify the channel wave numbers;  $E_{\text{cm}}$ ,  $E_{nli}$ , and  $E_{nl}$  are respectively the relative motion energy and bound energies of the exotic atom in the entrance and current channels. The basis used in the present study includes exotic atom states corresponding to both open ( $k_{nl}^2 > 0$ ) and closed ( $k_{nl}^2 < 0$ ,  $\text{Im } k_{nl} > 0$ ) channels.

The explicit analytical expression for a matrix

$$W_{n'l'L',nlL}^{Jp}(R) = \langle nl, L : JM|V(\boldsymbol{\rho}, \mathbf{R})|n'l', L' : JM\rangle \quad (11)$$

of the interaction potential,  $V(\boldsymbol{\rho}, \mathbf{R})$ , between the asymptotic initial  $|nlL; J\rangle$  and final  $|n'l'L'; J\rangle$  channels is obtained by integrating over  $\boldsymbol{\rho}$  and  $\hat{\mathbf{R}}$  without any additional approximations. As a result, the matrix elements (11) are reduced to the finite sum of multipole interactions  $W_{t;n'l',nl}(R)$  (allowed by the angular momentum and parity selection rules) with the asymptotic behavior:

$$W_{t;n'l',nl}(R) \propto R^t \quad (R \rightarrow 0) \quad (12)$$

and

$$W_{t;n'l',nl}(R) \propto \exp(-2R)/R^{t+1} \quad (R \rightarrow \infty), \quad (13)$$

where  $t$  is a multipolarity, which changes from  $t_{\min} = |l - l'|$  up to  $t_{\max} = l + l'$  (for details see Appendix A).

The scattering problem (9-11) was solved numerically by applying the propagator matrix method, developed earlier (for details see [31]), at each fixed value of the relative energy, total angular momentum and parity. In the frame of this method, instead of radial channel functions  $G_{nlL}^{EJp}(R)$ , we find their ratios in two nearest points  $R_i$  and  $R_{i+1}$  ( $R_{i+1} = R_i + h$ ;  $h$  is the constant integration step), starting from  $R_1 = 0$ . Then, using the two-point matching conditions, the  $K$  matrix, defined in the subspace of open channels ( $k^2 > 0$ ), and thereby the  $T$  matrix ( $T = -2iK(I - iK)^{-1}$ ) are calculated. The method allows to avoid numerical problems with both the exponentially growing and exponentially damping functions and significantly improves the accuracy of the calculated  $T$  matrix and correspondingly cross sections.

The degeneracy-averaged partial-wave differential cross sections for processes (1) are given by

$$\frac{d\sigma_{nl \rightarrow n'l'}^J}{d\Omega} = \frac{1}{2l+1} \frac{k_{n'l'}}{k_{nl}} \sum_{m,m'} |f_{nlm \rightarrow n'l'm'}^J(\Omega)|^2. \quad (14)$$

Here, the partial-wave on-shell scattering amplitudes,  $f_{nlm \rightarrow n'l'm'}^J(\Omega)$ , for the transition  $i \rightarrow f$  ( $i$  and  $f$  denote the quantum numbers of initial  $|nlm\rangle$  and final  $|n'l'm'\rangle$  states of exotic atom, respectively) are determined by the transition matrix  $T_{nlL \rightarrow n'l'L'}^J$ :

$$f_{i \rightarrow f}^J(\Omega) = \frac{i\sqrt{\pi}}{\sqrt{k_{nl}k_{n'l'}}} \sum_{L,L',\lambda'} i^{L'-L} \sqrt{2L+1} \langle lmL0 | Jm \rangle \times T_{nlL \rightarrow n'l'L'}^J \langle l'm'L'\lambda' | Jm \rangle Y_{L'\lambda'}(\Omega), \quad (15)$$

where the sums go over all values ( $L, L', \lambda'$ ), satisfying angular momentum and parity selection rules;  $\Omega = (\theta, \phi)$  is the center-of-mass solid angle.

The partial-wave integrated cross sections for  $nl \rightarrow n'l'$  transitions are given by

$$\sigma_{nl \rightarrow n'l'}^J = \frac{\pi}{k_{nl}^2} \frac{2J+1}{2l+1} \sum_{L,L'} |T_{nlL \rightarrow n'l'L'}^J|^2. \quad (16)$$

Then the total differential,

$$\frac{d\sigma_{nl \rightarrow n'l'}}{d\Omega} = \sum_{J=0}^{J_{\max}} \frac{d\sigma_{nl \rightarrow n'l'}^J}{d\Omega}, \quad (17)$$

and integrated,

$$\sigma_{nl \rightarrow n'l'} = \sum_{J=0}^{J_{\max}} \sigma_{nl \rightarrow n'l'}^J, \quad (18)$$

cross sections are obtained by summing (14) and (16) over partial waves from  $J = 0$  up to  $J_{\max}$  until an accuracy better than 0.01% was reached for all collisional energies.

The quantum-mechanical approach described above was applied to produce the systematic calculations of differential and integrated cross sections (14, 16 - 18) for processes (1) in collisions of excited  $\mu^-p$  and  $\mu^-d$  with ordinary  $H$  and  $D$  atoms, respectively. These calculations were performed using the basis, which includes all open and closed channels, associated with the principal quantum number values from  $n = 1$  up to  $n_{\max} = 20$ . In the case of the  $(\mu^-p)_{2s}$  and  $(\mu^-d)_{2s}$ , for a collision energy below  $2p$  threshold, the used basis was even extended up to  $n_{\max} = 30$ . Since the energies of  $ns$  and  $nl$  ( $l \geq 1$ ) sub-levels are split (mainly due to electron vacuum polarization), the cross sections with initial  $ns$  and  $nl$  ( $l \geq 1$ ) states were calculated separately for relative energies referring to  $ns$  and  $np$  thresholds. The results of our systematic calculations are extremely extensive and were used as input data for the detailed description of the atomic cascade kinetics.

Here, we present only the key points illustrating both the convergence of various cross sections (elastic scattering, Stark transitions, and CD) with the extension of the basis and the isotopic effect in the scattering of excited muonic hydrogen and deuterium. To demonstrate some of our results, the  $l$ -averaged cross sections of  $n \rightarrow n'$  ( $n' \leq n$ ) transitions, obtained by summing (18) over  $l'$  and averaging with the statistical weight  $(2l+1)/(n^2-1)$  over  $l \geq 1$  are defined as follows

$$\sigma_{n \rightarrow n'}^{\text{av}}(E) = \frac{\pi}{k_{nl}^2} \frac{1}{n^2-1} \sum_{l \geq 1, l'} (2l+1) \sigma_{nl \rightarrow n'l'}. \quad (19)$$

## B. The effect of closed channels in the scattering of excited muonic hydrogen atoms

In real applications of the close-coupling approach the used basis is always truncated. All the basis states associated with open channels are usually taken into account. The reliability of results obtained with this basis is unclear without the further study of the effect of closed channels. There are no simple theoretical representations or estimations, which allow to choose the optimal basis. Hence, the scattering problem has to be investigated numerically. This study is also necessary from the viewpoint of practical applications, to produce calculations within the reasonable computer time.

The extension of the basis set by adding muonic atom states associated with closed channels alters the effective interaction at short distances and, as a result, should affect the low-energy scattering of exotic atoms in the states with small values of the principal quantum number  $n$ . To study the closed channel effect and convergence of the close-coupling approach we have performed a lot of calculations with large basis sets. The key features of the closed channel effect in the scattering of the excited muonic hydrogen are demonstrated in Figs. 1 - 5.

Figure 1 shows the dependence of the partial-wave cross section ( $J = 0$ ) of the elastic  $2s - 2s$  scattering on  $E_{\text{lab}}$  which is the laboratory kinetic energy of muonic atom in its collision with target at rest. The calculations were performed for various basis sets corresponding to

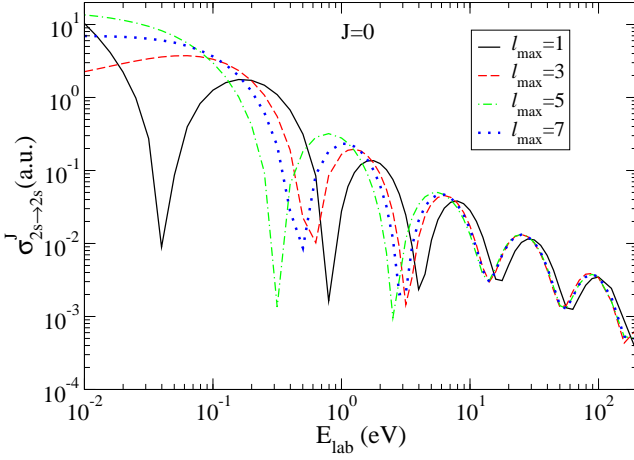


FIG. 1: (Color online) The partial-wave elastic cross section for  $(\mu^-p)_{2s} + H$  collision vs. the laboratory kinetic energy  $E_{lab}$  calculated for four variants of the basis corresponding to  $n_{max} = 8$  and different values  $l_{max}$  of the internal orbital momentum.

$n_{max} = 8$  and different values of the internal angular momentum  $l \leq l_{max}$  ( $l_{max} = 1, 3, 5, 7$ ). At the laboratory kinetic energy  $E_{lab} \lesssim 0.4$  eV (below the  $2p$  threshold) there are only two open channels associated with  $1s$  and  $2s$  states of the muonic hydrogen. All the other channels are closed: the weakly closed  $2p$  channel and strongly closed channels for  $n > 2$  (here the energy gap between the open and closed channels is more than a few hundred electron volts). At collision energies above the  $2p$  threshold the  $2p$  channel becomes also opened. Thus, the maximum number of open channels at energies above the  $2p$  threshold is three. In the case  $J = 0$  ( $L = l$  and parity  $p = 1$ ), the number of channels equals to the number of basis states. Therefore, for the basis with  $n_{max} = 8$  and  $l_{max} = 1$  or  $l_{max} = 7$  one has a 15-channel or 36-channel scattering problem, respectively.

The effective interaction in the system is very strong and leads to the formation of a number of bound states below  $2s$  threshold. This is confirmed by oscillations of the elastic cross section  $2s - 2s$  in Fig. 1 in accordance with Levinson's theorem. The extension of the basis increases the effective interaction (attraction at short distances) and as a consequence all maxima and minima in the cross section are shifted to lower energies.

Figure 2 shows the energy dependence of the partial-wave cross section ( $J = 0$ ) of the CD  $2s \rightarrow 1s$ . The calculations were performed for four variants of the basis corresponding to  $n_{max} = 8$  and different values of the internal angular momentum  $l \leq l_{max}$  ( $l_{max} = 1, 4, 5, 7$ ). Here the number of open and closed channels is determined by both the collision energy and the value of  $l_{max}$  as in the case of the elastic scattering  $2s - 2s$ .

As it is seen in Figs. 1 and 2, the effect of closed channels is very strong. The cross sections of the elastic scattering  $2s - 2s$  and CD  $2s \rightarrow 1s$  are essentially modified with the extension of the basis. The convergence is very slow. The lowest  $l$  orbitals are very important, but, as a rule, do not lead to a reliable result. Cross sections calculated by taking into account only  $ns$  and  $np$  states

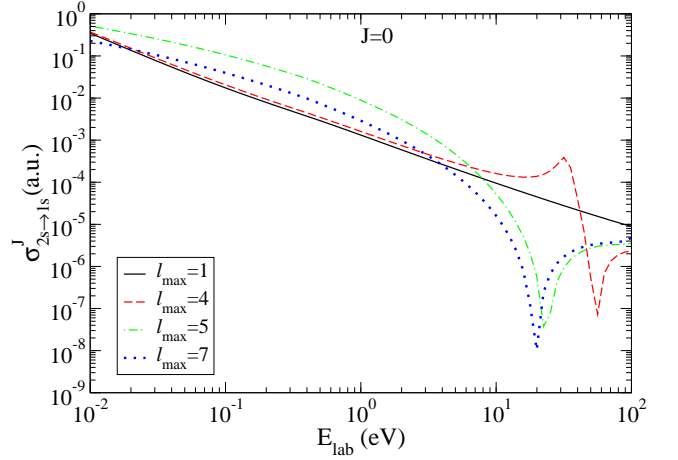


FIG. 2: (Color online) The same as Fig. 1 for the partial-wave cross section of the Coulomb de-excitation  $2s \rightarrow 1s$ .

differ substantially from those obtained with the further extension of the basis by including the states with large values of the internal orbital angular momentum ( $l \geq 2$ ). In particular, the extension of the basis results in the resonance behavior of both elastic  $2s - 2s$  and Coulomb  $2s \rightarrow 1s$  cross sections above  $E_{lab} \approx 20$  eV. The position and shape of this resonance essentially change with the extension of the basis (see Fig. 2). The results obtained with the basis sets corresponding to  $l_{max} = 6$  and  $7$  are indistinguishable for both elastic scattering and CD cross sections.

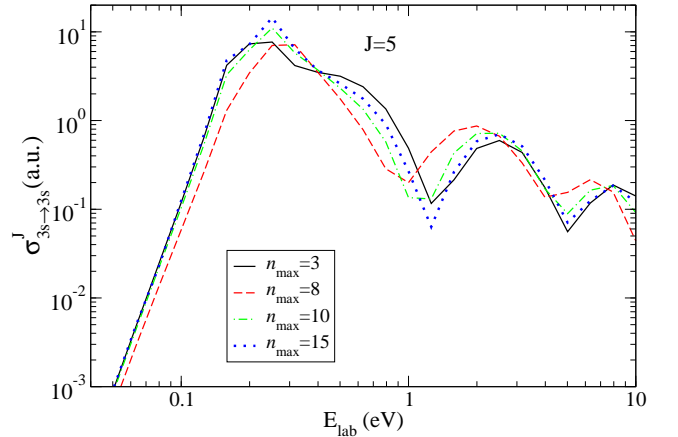


FIG. 3: (Color online) The energy dependence of the partial-wave elastic cross section for  $(\mu^-p)_{3s} + H$  collision calculated with the basis corresponding to different values  $n_{max}$ .

The convergence of the partial-wave ( $J = 5$ ) cross sections of the elastic  $3s - 3s$  scattering and the CD  $3s \rightarrow 2s$  of the muonic hydrogen with the extension of the basis (by increasing  $n_{max}$ ) is demonstrated in Figs. 3 and 4, respectively. Calculations were done for different basis sets corresponding to muonic hydrogen states with  $n_{max}=3, 8, 10, 15, 20$  and all values of the internal orbital angular momentum at a given  $n_{max}$ .

The closed channel effect is very noticeable in the case of the elastic scattering (see Fig. 3). The partial-wave cross section of the elastic  $3s - 3s$  scattering changes with

the extension of the basis from  $n_{\max} = 3$  to  $n_{\max} = 8$  about a few times near its values calculated with the minimal basis ( $n_{\max} = 3$ ), however, its energy behavior is conserved. Further enlargement of basis set leads to the convergence of the calculated cross section as shown in Fig. 3 (see curves corresponding to  $n_{\max} = 10$  and  $n_{\max} = 15$ ). Note that the results of the calculation with a basis set  $n_{\max} = 20$  practically coincide with those obtained with the basis  $n_{\max} = 15$  and not shown in Fig. 3.

In the case of the CD (see Fig. 4) the effect is much stronger. The extension of the basis leads to a significant

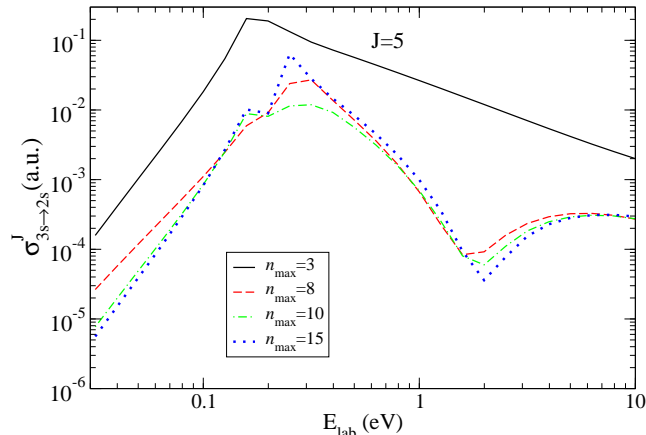


FIG. 4: (Color online) The same as Fig. 3 for the partial-wave cross section of the Coulomb de-excitation  $3s \rightarrow 2s$ .

reduction of the cross section of the CD  $3s \rightarrow 2s$  (more than one order of magnitude) and, as in the case of the Coulomb  $2s \rightarrow 1s$  de-excitation (see Fig. 2), its energy dependence changes as well. As in the case of the elastic scattering  $3s - 3s$ , the convergence of the partial-wave CD  $3s \rightarrow 2s$  cross section is achieved with the basis set corresponding to  $n_{\max} = 15$  and further extension of the basis set to  $n_{\max} = 20$  leads to variation of the cross section less than 1%.

TABLE I: The maximum number of closed channels in calculations of elastic  $3s - 3s$  scattering and CD  $3s \rightarrow 2s$  for different basis sets and  $J$  values.

$n_{\max}$	3	8	12	20
$J = 5$	0	106	298	754
$J = 10$	0	110	353	959

In the considered examples of the elastic  $3s - 3s$  scattering and the CD  $3s \rightarrow 2s$  at the collision energy above  $3p$  threshold ( $E_{\text{lab}} \gtrsim 0.125$  eV) one has 10 open channels. The number of the closed channels essentially depends on both  $n_{\max}$  and  $J$  values. It is important to note, that with increasing  $J$  the number of closed channels increases significantly (see Table 1).

Figure 5 shows the energy dependence of integrated cross sections for  $(\mu^- p)_{3s} + H$  collisions. Here we present numerical results for the elastic scattering  $3s - 3s$ , Stark transition  $3s \rightarrow 3p$ , and CD  $3s \rightarrow 2s$  and  $3s \rightarrow 1s$ .

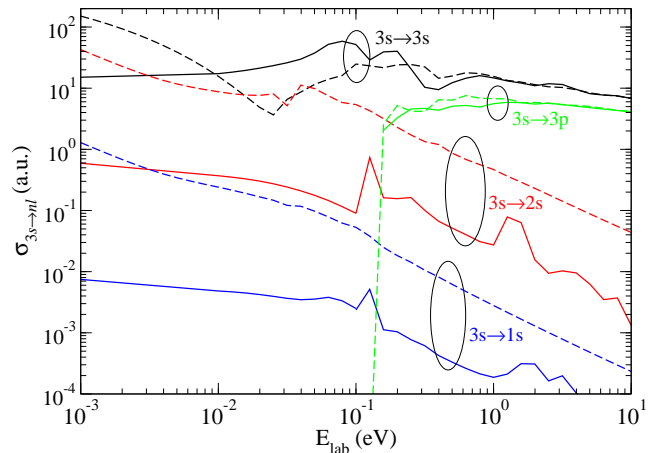


FIG. 5: (Color online) The energy dependence of the integrated cross sections for  $(\mu^- p)_{3s} + H$  collisions calculated with different basis sets:  $n_{\max} = 3$  (dashed lines) and  $n_{\max} = 20$  (solid lines).

Calculations were performed for two variants of the used basis: the minimum basis set ( $n_{\max} = 3$ ) and the maximum basis set including all the muonic atom states associated with  $n \leq 20$ . The comparison of the results obtained in these two variants shows, that the closed channels strongly affect all cross sections at collision energies below a few electron volts. In particular, the cross section of the elastic scattering  $3s - 3s$  changes its energy dependence at low energies with the extension of the basis. A much stronger effect is observed in the case of the CD. The cross sections of  $3s \rightarrow 2s$  and  $3s \rightarrow 1s$  CD are reduced more than an order of magnitude with the extension of the basis at all energies under consideration.

Our investigation shows, that the convergence of cross sections with the extension of the basis is achieved very slowly in the lowest partial waves and at low-energy collisions due to a strong coupling between closed and open channels. The closed channel effect is especially significant in the low-energy scattering of exotic atoms in low-lying excited states ( $n = 2 - 5$ ), because the basis of the open channels is very poor to produce the reliable results (e.g., see Fig. 4 in [31]).

The present as well as our previous studies [31] show, that the energy dependence of the cross sections at low-energy collisions is very important for the kinetics of the atomic cascade. Therefore, the cross sections of different processes in the low-energy region should be calculated using the extended basis set, which includes a lot of closed channels. All our further calculations are performed using a basis set of  $n_{\max} = 20$ , the use of which allows to achieve the convergence of all cross sections in the whole energy range. Used basis set contains hundreds or even thousands of states depending on the values of the total angular momentum of the system. According to the present study, in the case of the muonic deuterium the convergence is achieved much faster than in the case of muonic hydrogen. Nevertheless, all calculations for both muonic hydrogen and muonic deuterium were performed with the same basis set corresponding to  $n_{\max} = 20$ .



### C. $J$ -dependence of different cross sections

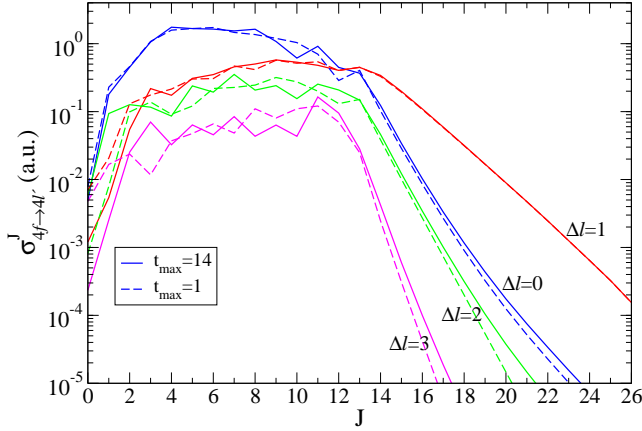


FIG. 6: (Color online) The partial-wave elastic  $4f-4f$  and Stark  $4f \rightarrow 4l$  ( $l = 0-2$ ) cross sections for  $(\mu^-p)_{4f} + H$  collision vs. the total angular momentum  $J$  at the laboratory kinetic energy  $E_{\text{lab}} = 1$  eV. The calculations were performed with the basis set including all the exotic atom states with principal quantum numbers  $n \leq 20$  ( $\Delta l = |l_i - l_f|$ ) for two variants of interaction potentials:  $t_{\text{max}} = 14$  (solid lines) and  $t_{\text{max}} = 1$  (dashed lines).

Figure 6 shows the  $J$ -dependence of cross sections for the elastic  $4f-4f$  scattering and Stark  $4f \rightarrow 4l$  ( $l = 0-2$ ) transitions calculated at the laboratory kinetic energy  $E_{\text{lab}} = 1$  eV. In these calculations the basis includes all the exotic atom states with principal quantum numbers from  $n = 1$  up to 20 (note, that all channels associated with  $n \geq 5$  are closed). The behavior of partial-wave cross sections in the range of the total angular momentum  $J < J^*$  ( $J^* \approx 13$  at  $E_{\text{lab}} = 1$  eV) is quite similar. It is noteworthy, that the value of  $J^*$  grows with the increase in the principal quantum number (in the entrance channel) and a collision energy.

The partial-wave cross section of the elastic scattering is, on average, significantly larger (about one order of magnitude) than the partial-wave cross sections of Stark transitions ( $\Delta l = |l_i - l_f| \geq 1$ ).

At higher values of the total angular momentum  $J > J^*$  all the partial-wave cross sections rapidly decrease. The rate of this decrease essentially depends on the  $\Delta l$  value. The partial-wave cross sections of Stark transitions with the  $\Delta l = 1$  decrease much slower than the partial-wave cross sections of the elastic scattering ( $\Delta l = 0$ ) and Stark transitions with  $\Delta l \geq 2$ . Such a behavior of partial-wave cross sections is explained in the case of transitions with  $\Delta l = 1$  by the direct dipole ( $t = 1$ ) coupling (see (13)) between entrance and final channels, whereas in the  $\Delta l \neq 1$  case the corresponding cross sections are mainly determined by the effective dipole coupling through intermediate states.

This conclusion is confirmed in Fig. 6, where the same cross sections were calculated for two variants of interaction potentials. In the first variant the matrix of interaction potentials includes only monopole and dipole terms ( $t_{\text{max}} = 1$ ), whereas in the second variant all the allowed multipoles up to  $t_{\text{max}} = 14$  were taken into ac-

count. For transitions with  $\Delta l = 1$  the direct dipole interaction ( $t = 1$ ) determines the coupling between initial and final channels and very accurately reproduces the  $J$ -dependence of Stark cross sections with  $\Delta l = 1$ . Here the higher multipoles with  $t \geq 2$  practically do not change this cross section (see Fig. 6). In the case of transitions with  $\Delta l \geq 2$  the direct interaction with  $t \geq 2$  gives a noticeable contribution only at small  $J$ , whereas the effective dipole coupling largely determines both the value of the corresponding cross section and its  $J$ -dependence at large  $J$  values, as shown in Fig. 6.

The fast decrease of the partial-wave cross sections with the increase in the total angular momentum at  $J > J^*$  is a general feature, which is also revealed in partial-wave cross sections of both elastic scattering (e.g.,  $4s-4s$ ,  $4p-4p$ , and  $4d-4d$ ) and Stark transitions with a fixed  $\Delta l$  for the given  $n$ .

Figure 7 shows the  $J$ -dependence of partial-wave cross sections for different Coulomb transitions ( $\Delta n = n_i - n_f = 1-3$ ) in  $(\mu^-p)_{4l} + H$  collisions. Calculations were performed with the basis including all the exotic atom states with  $n \leq 20$  at the laboratory kinetic energy  $E_{\text{lab}} = 1$  eV. The present study shows that, in contrast

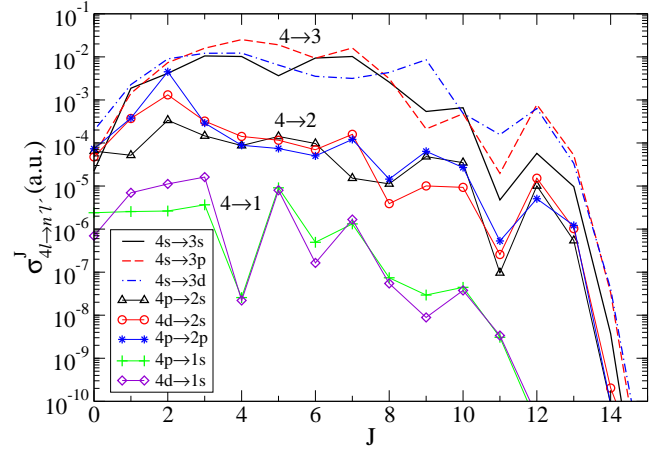


FIG. 7: (Color online) The partial-wave CD cross sections for  $(\mu^-p)_{4l} + H$  collisions vs. the total angular momentum  $J$  calculated at the laboratory kinetic energy  $E_{\text{lab}} = 1$  eV with the basis including all the exotic atom states with  $n \leq 20$ .

to the convergence with respect to  $J_{\text{max}}$  observed above in Fig. 6, the partial-wave cross sections of the CD (see Fig. 7) very sharply decrease at  $J_{\text{max}} \gtrsim 12$  for  $4 \rightarrow 3$ ,  $4 \rightarrow 2$ , and  $4 \rightarrow 1$  transitions independently from  $\Delta l$ . Such a behavior of CD cross sections is explained by the affect of the centrifugal barrier, which prevents partial waves with  $J_{\text{max}} \gtrsim 12$  (at a given energy  $E_{\text{lab}} = 1$  eV) from penetrating into the interaction range, where the process of the CD mainly occurs.

The fast decrease of partial-wave cross sections (see Figs. (6-7)) with the increase in the total angular momentum in the range  $J > J^*$  is a general property, manifested also in partial-wave cross sections of elastic scattering, Stark transitions, and CD at all the collision energies and for all the excited states of an exotic atom.

The comparison of the results shown in Fig. 6 and Fig. 7 allows to explain the different  $J$ -dependence of

partial-wave cross sections in Fig. 6 at  $J > J^*$ . In this range of  $J$ -values the coupling between open channels corresponding to the CD and closed channels can be neglected and calculations with the minimum basis set ( $n_{\max} = 4$  in the considered example) allow to obtain results which are in correspondence with the extended basis case. The cross sections of Stark transitions with  $\Delta l = 1$  are largely determined by the direct dipole coupling and survive for much larger  $J$  values in comparison with processes corresponding to  $\Delta l \neq 1$ . These observations allow significantly to reduce the dimension of the system of close-coupling equations and as a consequence the computer time.

#### D. Isotopic effect in the scattering of excited $\mu^-p$ and $\mu^-d$ atoms

As far as we know, the calculations of scattering cross sections for  $(\mu^-d)_n + D$  collisions in the framework of a fully quantum-mechanical approach have not been done so far and the isotopic effect in the scattering of the muonic atoms of hydrogen and deuterium has not been investigated either. In the present study the cross sections of elastic scattering, Stark transitions and CD for both muonic hydrogen and deuterium were calculated within the same fully quantum-mechanical approach. Calculations were performed using basis states corresponding to  $n_{\max} = 20$  and  $l \leq l_{\max} = n_{\max} - 1$ . This allows to study the isotopic effect in the scattering of the excited muonic hydrogen and deuterium on the same footing.

Figures 8 - 10 show the energy dependence of  $l$ -averaged cross sections for  $(\mu^-p)_n + H \rightarrow (\mu^-p)_{n'} + H$  and  $(\mu^-d)_n + D \rightarrow (\mu^-d)_{n'} + D$  collisions ( $n' \leq n$ ) with values of the principal quantum number  $n = 4, 5$ , and 8. The comparison of the results obtained for the muonic

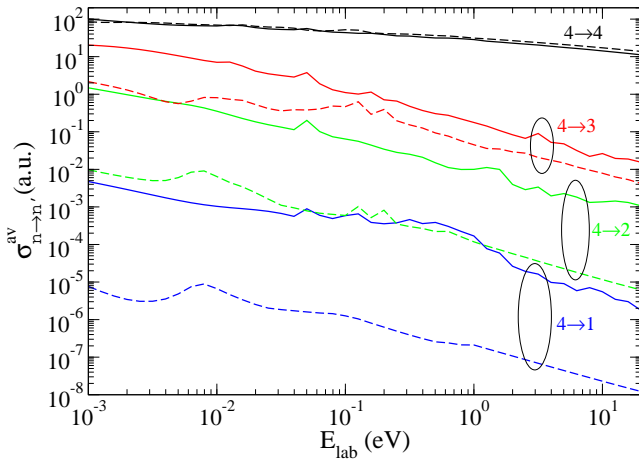


FIG. 8: (Color online) The  $l$ -averaged cross sections for  $(\mu^-p)_n + H \rightarrow (\mu^-p)_{n'} + H$  (solid lines) and  $(\mu^-d)_n + D \rightarrow (\mu^-d)_{n'} + D$  (dashed lines) collisions ( $n = 4$ ) vs. the laboratory kinetic energy  $E_{\text{lab}}$ .

hydrogen and deuterium reveals, that the  $l$ -averaged cross sections without changing the principal quantum number differ not more than (10 -15)%. At all collision

energies these cross sections in the case of the  $(\mu^-d)_n + D$  scattering are slightly more than in the  $(\mu^-p)_n + H$  one.

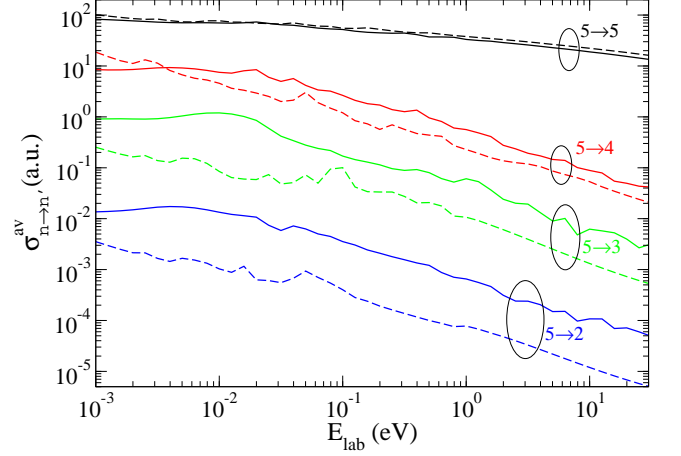


FIG. 9: (Color online) The same as in Fig. 8 for  $n = 5$ .

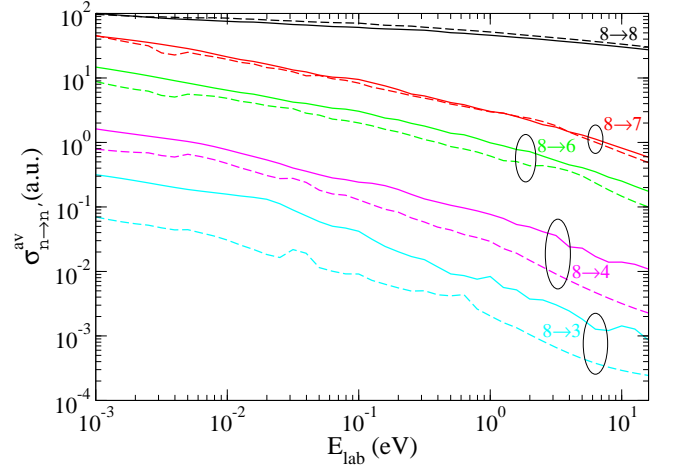


FIG. 10: (Color online) The same as in Fig. 8 for  $n = 8$ .

Unlike the  $l$ -averaged cross sections of Stark transitions, a much stronger isotopic effect is observed in  $l$ -averaged cross sections of the CD ( $n \rightarrow n' \leq n - 1$ ). For a given  $n$  value and fixed  $\Delta n = n - n'$  the cross section of the CD in the case of  $(\mu^-d)_n + D$  collision is always less than in the case of  $(\mu^-p)_n + H$  collision and this difference grows essentially with increasing  $\Delta n$ , as shown in Figs. 8 - 10. On the other hand, the isotopic effect decreases with the increase in the principal quantum number of the initial state. In particular, the  $l$ -averaged cross sections of the CD  $8 \rightarrow 7$  of the muonic hydrogen and deuterium are almost indistinguishable on eye, while in the case of the  $l$ -averaged cross sections of CD  $5 \rightarrow 4$  and especially  $4 \rightarrow 3$  the isotopic effect is very strong.

The suppression of the cross sections of CD in the case of the muonic deuterium as compared with the muonic hydrogen is mainly explained by the weakening of the effective coupling,  $W_{n'l'L',nlL}^{Jp}(R)G_{n'l'L'}^{EJp}(R)$  (see 9), between open channels as well as between open and closed channels. At a fixed energy the ratio of the absolute



values of wave numbers of the scattering problem is determined mainly by the reduced masses of the system. In the scattering of  $\mu d$  and  $\mu p$  atoms it is equal to  $|k_{nl}(\mu d)/k_{nl}(\mu p)| \approx 1.4$ . Therefore, in the case of the muonic deuterium the wave functions of closed channels are exponentially damped at smaller distances, and the wave functions of open channels respectively oscillate much faster. Both these factors lead to a significant weakening of the effective coupling between different channels and, as a consequence, a significant suppression of CD cross sections.

The interplay of various processes in the kinetics of the atomic cascade is determined by their rates. The rates of collisional processes in the laboratory frame are defined as follows

$$\lambda_{nl \rightarrow n'l'}(E_{\text{lab}}) = \varphi N_{\text{LHD}} \sigma_{nl \rightarrow n'l'}(E_{\text{lab}}) \sqrt{\frac{2E_{\text{lab}}}{M_{\mu a}}}, \quad (20)$$

where  $\varphi = N/N_{\text{LHD}}$  is the relative density of the target in the units of the liquid hydrogen density,  $N_{\text{LHD}} = 4.25 \times 10^{22}$  atoms/cm<sup>3</sup> and  $E_{\text{lab}}$  is a laboratory kinetic energy of a muonic atom. While  $\mu$ -decay and radiative transition rates do not depend on the kinetic energy of the muonic atom, target density, and temperature, the rates of collisional processes essentially depend on these physical parameters.

The energy dependence of  $l$ -averaged CD rates

$$\lambda_{n \rightarrow n'}^{\text{av}}(E_{\text{lab}}) = \varphi N_{\text{LHD}} \sigma_{n \rightarrow n'}^{\text{av}}(E_{\text{lab}}) \sqrt{\frac{2E_{\text{lab}}}{M_{\mu a}}}, \quad (21)$$

for  $(3 \rightarrow 2)$  and  $(4 \rightarrow 3)$  transitions in muonic hydrogen and deuterium calculated at a liquid hydrogen density ( $\varphi = 1$ ) are shown in Figs. 11 and 12 together with the rates  $\lambda^{\text{rad}}(np \rightarrow 1s)$  of radiative transitions  $(3p \rightarrow 1s)$  and  $(4p \rightarrow 1s)$ , respectively. A small difference between the radiative rates of  $(np \rightarrow 1s)$  transitions in muonic hydrogen and deuterium due to their reduced masses is not visible at the scale of Figs. 11 and 12.

Here the isotopic effect revealed in cross sections (see Figs. 8 - 10) is additionally enhanced by the trivial kinematic factor associated with the difference of exotic atom velocities at a fixed energy in the laboratory system (due to the different masses of muonic hydrogen and deuterium atoms). The isotopic effect is very strong and significantly changes the rates of CD especially in the low-energy region. In particular, this effect results in decreasing the rate of the CD  $(5 \rightarrow 4)$  more than four times (see Fig. 9), about an order of magnitude the rate of the CD  $(4 \rightarrow 3)$ , and even much more the rate of the CD  $(3 \rightarrow 2)$  in the case of the  $(\mu^- d)$  atom, as compared with the case of the  $(\mu^- p)$  atom. Comparing the rates of CD  $(3 \rightarrow 2)$  and  $(4 \rightarrow 3)$  respectively with radiative transition rates  $(3p \rightarrow 1s)$  and  $(4p \rightarrow 1s)$ , we can conclude that the acceleration of the muonic hydrogen due to CD should be more significant than in the muonic deuterium case. This isotopic effect has to lead to the much lesser Doppler broadening of the  $K$  lines in the case of the muonic deuterium in comparison with the case of the muonic hydrogen. This effect must be especially noticeable at the relative density above  $\varphi \approx 10^{-3}$ .

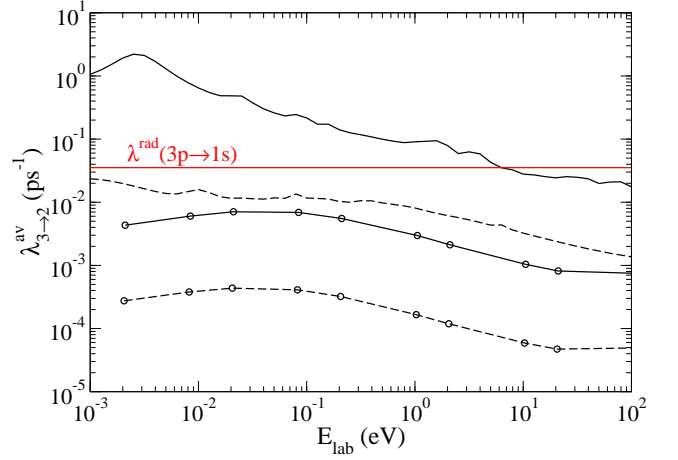


FIG. 11: (Color online) The  $l$ -averaged Coulomb  $3 \rightarrow 2$  de-excitation rates calculated at the liquid hydrogen density ( $\varphi = 1$ ) for muonic hydrogen (solid line) and deuterium (dashed line) atoms vs. the laboratory kinetic energy  $E_{\text{lab}}$ . The curves with open circles are from [26]. The horizontal line shows the rate of the radiative  $3p \rightarrow 1s$  transition in both muonic hydrogen and deuterium (see the text).

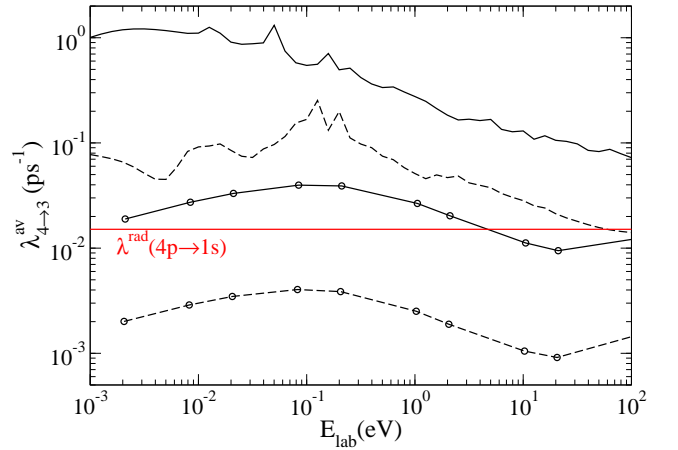


FIG. 12: (Color online) The same as in Fig. 11 for Coulomb  $4 \rightarrow 3$  de-excitation rates vs. the laboratory kinetic energy  $E_{\text{lab}}$ . The curves with open circles are from [26]. The horizontal line shows the rate of the radiative  $4p \rightarrow 1s$  transition in both muonic hydrogen and deuterium.

The comparison of the present results with those obtained in the framework of the asymptotic theory of non-adiabatic transitions (see [26] and references therein) is given in Figs. 11 and 12. It is seen, that the rates of the CD from paper [26] only qualitatively reproduce the isotopic effect, but they are too small to explain the experimental data (e.g., see [7, 13]). It should be noted that all the previous calculations of the CD were realized within semiclassical or adiabatic approaches with a two-level approximation which is not suitable for the treatment of the deeply inelastic process such as CD (e.g., see [28, 38]).

The observed isotopic effect in both cross sections and the rates of the CD allows to predict a similar effect in the pionic deuterium and the muonic tritium. This effect should lead to a strong weakening of the high-energy

components in the energy spectrum of the pionic deuterium and especially in the case of the muonic tritium compared to the pionic and muonic hydrogen atoms, respectively. In particular, the predicted isotopic effect allows for the first time to explain the significant suppression of the contributions of high-energy components originating from CD transitions ( $4 \rightarrow 3$ ) and ( $5 \rightarrow 3$ ) in shift/width experiments [39] with the pionic deuterium.

### III. KINETICS OF THE ATOMIC CASCADE

The life history of the exotic atom after its formation is determined by the complex interplay of collisional and non-collisional processes. In these processes the initial distributions on quantum numbers  $(n, l)$  and the laboratory kinetic energy  $E$  (at the instant of the exotic atom formation) change during the de-excitation cascade until the exotic atom arrives in the ground state or the weak decay (absorption or annihilation in the case of hadronic atoms) of the exotic particle occurs.

The theoretical predictions of various characteristics of the atomic cascade represent an idealized view of what one might expect in experimental studies, because they are free from standard experimental problems associated with the energy resolution, efficiency of the registration, statistic, and so on. Besides, the model representations used in the analysis of experimental data may also lead to additional uncertainties. Hence, the reliable theoretical predictions may be very useful both for choosing the optimal conditions of experiments and improving the results extracted from the analysis of experimental data.

The evolution of the kinetic energy and  $(n, l)$  distributions of exotic atoms plays a significant role in the competition of various cascade processes and should be followed up during the whole atomic cascade. To realize this, the comprehensive sets of differential and integrated cross sections of collisional processes, involved in the atomic cascade, were calculated (in a framework of the present quantum-mechanical approach) in the wide range of quantum numbers ( $n \leq 8$ ) and kinetic energies of muonic atoms, that are of interest to reliable cascade calculations. Besides, the realistic model simulating the kinetics of the atomic cascade was developed. It is especially important from the viewpoint of various precise experiments with muonic [10, 13, 14, 40–45] and hadronic [1–3, 15, 39, 46–51] hydrogen atoms.

For the collisions of highly excited exotic atoms ( $n > 8$ ) with molecular hydrogen the results of the classical-trajectory Monte Carlo calculations [24] were used. It is important to note that the isotopic effect revealed in the cross sections for scattering of muonic atoms in states with  $n < 9$ , is virtually nonexistent in their scattering in highly excited states with  $n > 9$ . The only source of the isotopic effect in the kinetics of atomic cascade here is a trivial kinematic factor of the transition from the cross sections of processes to their rates.

#### 1. Cascade processes

In the present paper we use as the improved version of the ESCM originally developed in [11] and later essentially improved in the paper [12] and in recent papers [31, 52, 53]. The improvements were mainly achieved due to new theoretical results for the cross sections of the collisional processes and initial distributions of muonic atoms in the quantum numbers and the laboratory kinetic energy at the instant of their formation. The ESCM includes: radiative transitions, CD, external Auger effect, and Stark transitions, as well as the elastic scattering and  $\mu^-$  - decay.

The most known cascade process, beyond the  $\mu^-$  - decay, is the radiative  $n_i l_i \rightarrow n_f l_f$  de-excitation described by electro-dipole transitions, in which the initial and final values of the internal orbital angular momentum of exotic atoms satisfy the selection rule  $\Delta l = |l_i - l_f| = 1$ . The rates of radiative transitions are calculated with very high accuracy and together with the  $\mu^-$  - decay almost entirely determine the de-excitation cascade at very low target densities  $\varphi \lesssim 10^{-7}$ . In this density range the information about initial  $n$ -,  $l$ -, and  $E$ -distributions is practically conserved up to the end of the cascade (e.g., see [31]).

At higher densities the collisional processes become very important, because their rates are proportional to the target density and, as a rule, have a strong energy dependence. The external Auger effect, elastic scattering, Stark transitions, and CD are the main collisional processes determining the data observed or extracted from various experiments.

The external Auger effect does not change the kinetic energy of the exotic atom, because the transition energy is practically carried away by the target electron. The Auger transitions with the minimal  $\Delta n = n_i - n_f$  needed for the ionization of the target are the most probable. The rates of the external Auger effect reach their maximum at  $\Delta n = 1$  (the transition  $7 \rightarrow 6$  in the muonic atom case) and they rapidly decrease both for  $n < 7$  and  $\Delta n > 1$ . The cross sections of the external Auger effect were calculated in the semiclassical approximation and used through the whole cascade.

The elastic scattering, Stark transitions and CD significantly change both the kinetic energy and quantum numbers of exotic atoms. The Stark transitions affect the population of  $nl$  sub-levels and together with the elastic scattering, as a rule, decelerate exotic atoms, thus changing the interplay of different de-excitation processes during the atomic cascade. The process of the CD plays a very important role in the acceleration of exotic atoms. In this process the energy of the transition  $n \rightarrow n' < n$  is converted into the kinetic energy of the relative motion and shared between colliding objects (exotic and target atoms).

The competition of the external Auger effect and the CD significantly depends on both the initial state of the muonic atom and its kinetic energy. In addition, their interplay differs for muonic hydrogen and deuterium atoms, due to the isotopic effect mainly in the CD of these muonic atoms. The energy dependence of the ratio of

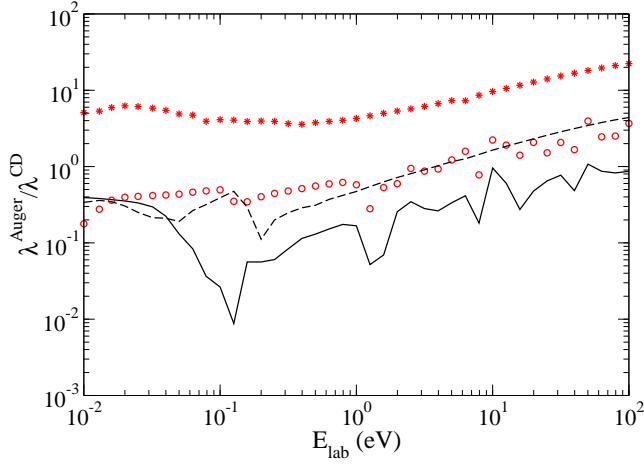


FIG. 13: (Color online) The ratio of the external Auger effect and CD rates,  $\lambda^{Auger}/\lambda^{CD}$ , vs. the laboratory kinetic energy calculated for  $\mu^-p$  and  $\mu^-d$  atoms in the  $3s$  state (solid and dashed lines, respectively) and in the  $3p$  state (open circles and asterisk, respectively).

the external Auger effect and CD rates calculated for  $\mu^-p$  and  $\mu^-d$  atoms in  $3s, 3p$  states and in  $5s, 5p$  states is shown in Figs. 13 and 14, respectively. As can be seen, this ratio has a nontrivial energy dependence which essentially depends on the exotic atom state. The competition between these processes significantly affects the energy distribution of muonic atoms, in particular, appears in the spectra of muonic atoms at the time of radiative transitions (e.g., see Figs. 20 and 21 below).

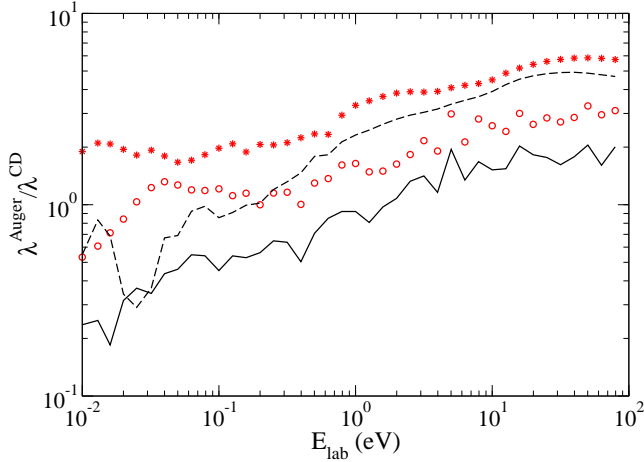


FIG. 14: (Color online) The same as in Fig. 13 for  $\mu^-p$  and  $\mu^-d$  atoms in the  $5s$  state (solid and dashed lines, respectively) and in the  $5p$  state.

According to our knowledge, a fully quantum mechanical calculations of the cross sections of the charge-exchange process and the external Auger reaction with the formation and subsequent decomposition of the intermediate molecular complex is currently lacking. Estimates of the cross sections (rates) of these processes (e.g., see [26, 27, 54] and references therein) allow us to conclude that their role in the kinetics of atomic cascade is insignificant in comparison with the direct Coulomb

de-excitation and Auger ionization of the target atom. Thus, the above mentioned processes are not taken into account in the present version of the ESCM.

## 2. Initial distributions and the thermal motion of the target

The simplest model of the exotic atom formation, usually used in cascade calculations, is based on the assumption, that the exotic atoms are formed in states with a fixed principal quantum number  $n = n_0 \approx \sqrt{m_r}$  ( $\approx 14$  for muonic hydrogen) and the statistical  $l$  distribution  $(2l+1)/n_0^2$  ( $l \leq n_0 - 1$ ) of  $n_0l$  sub-levels (e.g., see [12] and references therein). This simple representation of the exotic atom formation is not confirmed by more elaborated studies [55–57], in which the molecular structure of the target was taken into account. According to these studies, the muonic atoms are formed in states with a broad distribution in the principal quantum number, the maximum of which is shifted to lower  $n \cong 11 < n_0$ . Besides, the populations of  $nl$  sub-levels have a non-statistical distribution over  $l$  for each value of the principal quantum number.

In the present cascade model the initial  $n$ -,  $l$ -, and  $E$ - distributions are assumed to be factorized as in our previous papers [19, 31, 53]. The probability densities of initial  $n$ - and  $l$ - distributions (denoted by  $f_n$  and  $f_l$ , respectively) as well as of the initial kinetic energy distribution  $\omega_{in}(E)$  were assumed to be the same for both muonic hydrogen and deuterium atoms.

Here we use:

- the Gaussian  $n$ -distribution

$$f_n \propto e^{-\alpha_n(n-n_0)^2}, \quad (22)$$

centered at  $n_0 = 11$  ( $\alpha_n = 0.5$ );

- the modified statistical  $l$ -distribution

$$f_l \propto (2l+1)e^{-\alpha_l(2l+1)} \quad (23)$$

( $\alpha_l = 0.08$ ) for each value of the principal quantum number  $n$ ;

- the two-exponential  $E$ -distribution

$$\omega_{in}(E) = \frac{\varkappa}{E_1} \exp\left(-\frac{E}{E_1}\right) + \frac{1-\varkappa}{E_2} \exp\left(-\frac{E}{E_2}\right), \quad (24)$$

where parameters  $E_1 = 0.469$  eV,  $E_2 = 4.822$  eV, and  $\varkappa = 0.805$  have been determined in [31] by fitting experimental data [10] obtained at the target pressure  $p_{H_2} = 0.0625$  hPa and room temperature. In the present study these initial distributions were used for both muonic hydrogen and deuterium atoms at all target densities and temperatures.

## 3. The thermal motion of the target and kinematics of the binary collision

The thermal motion of the target is very important and should be taken into account in the realistic description of the kinetics of the atomic cascade. There are, at least, three main reasons to do it in a proper way. First, the

cross sections (or rates) of collisional processes have a strong energy dependence especially at low energies (e.g., see Figs. 8 - 12). Second, during the atomic cascade the kinetic energy of the exotic atom may be comparable with the energy of the thermal target motion. Finally, it is necessary for the exact knowledge about possible collisional processes and their correct description nearby  $ns - nl$  ( $l \geq 1$ ) thresholds.

In the present research, the exact relations between kinematic characteristics in the laboratory and center-of-mass systems *before and after the binary collision* were obtained and used in cascade calculations. In contrast to the case of the target at rest considered in the literature, the energy  $E_{cm}$  of the relative motion *before the collision* depends on both energies of colliding subsystems and azimuthal angle  $\chi$  of the collision in the laboratory system in the following way

$$E_{cm} = \frac{1}{M}(M_t E + M_{\mu a} E_t - 2\sqrt{M_t M_{\mu a} E E_t} \cos \chi). \quad (25)$$

Here,  $M_{\mu a}$  and  $M_t$  are masses of exotic and target atoms,  $M = M_t + M_{\mu a}$ ;  $E$  and  $E_t$  are kinetic energies of exotic and target atoms in the laboratory system before the collision. In the present cascade calculations we assume the uniform distribution of the azimuthal angle  $\chi$ . Besides, the thermal motion of the target is described by a Maxwell distribution,

$$F(E_t) = \frac{2}{\sqrt{\pi}} \sqrt{\frac{E_t}{(kT)^3}} \exp\left(-\frac{E_t}{kT}\right), \quad (26)$$

where  $T$  is the target temperature and  $k$  is the Boltzmann constant.

To obtain the kinetic energy of the muonic atom in the laboratory system *after the collision*, we apply the three-dimension geometry and the conservation laws of the energy and momentum. As a result, the following formula for the kinetic energy of the muonic atom in the laboratory system after the collision was derived

$$E' = \frac{1}{M} \{ M_t E'_{cm} + M_{\mu a} (E + E_t - E_{cm}) + [M_{\mu a} (E_{cm} - E_t) + M_t (E - E_{cm})] \sqrt{E'_{cm}/E_{cm}} \cos \theta \}. \quad (27)$$

Here,  $\theta$  is the scattering angle in the center-of-mass system,  $E'_{cm} = E_{cm} + \Delta_{if}$  is the kinetic energy of the relative motion after the collision, with  $\Delta_{if} = E_{n_i l_i} - E_{n_f l_f}$  being the difference of the bound energies of muonic atom states before and after the collision. It is noteworthy, that in the case of the external Auger effect the released energy is mainly carried away by the electron and in cascade calculations we neglect the recoil energy obtained by the muonic atom, hence,  $E = E'$ .

#### 4. Simulation of the atomic cascade

In the represented model of the atomic cascade the life history of each muonic atom can be traced from the moment of its formation until the transition to the ground

state or  $\mu^-$ -decay. A multi-step sequence randomly selected events, which simulate the kinetics of the atomic cascade, can be schematically described as follows:

- At the very beginning of the cascade the initial values of quantum numbers ( $n_i, l_i$ ) and the laboratory kinetic energy  $E$  of the muonic atom are randomly chosen according to their distributions Eqs. (22)-(24);

- Further, the kinetic energy  $E_t$  of the target (at a fixed target temperature) in accordance with Eq. (26) and the azimuthal angle  $\chi$  of the collision (in the laboratory system) are randomly chosen and the relative motion energy  $E_{cm}$  (before the collision) is calculated according to Eq. (25);

- The rates of collisional processes for a given  $E_{cm}$  together with the rates of radiative transitions and  $\mu$ -decay are used to calculate their total and relative rates (probabilities) at chosen above values of  $n_i, l_i, E_{cm}$  for all possible final states;

- In accordance with these relative rates, the event type and the quantum numbers ( $n_f, l_f$ ) of the final state are randomly chosen. In the case of collisional process, the scattering angle is randomly chosen in accordance with the angular distribution for a given process.

- As a result of these random events, one gets the type of the process, quantum numbers ( $n_f, l_f$ ) of the final state, and the new value of the laboratory kinetic energy  $E'$  of the muonic atom after the collision calculated according to Eq. (27). These new values ( $n_f, l_f, E'$ ) are used as initial ones and the simulation of the atomic cascade continues until  $\mu^-$ -decay occurs or the ground state of the muonic atom is reached.

The present cascade calculations for muonic hydrogen and deuterium atoms were performed in the relative density range, covering eight orders of magnitude ( $\varphi = 10^{-8} - 1$ ). To obtain good statistics, the destiny of the  $10^7$  muonic atoms have been analyzed in cascade calculations for each value of the target density and temperature. The various characteristics of the de-excitation cascade in muonic hydrogen and deuterium were calculated: the absolute and relative  $x$ -ray yields of different  $K_i$  ( $i = \alpha, \beta, \gamma$ , etc.) lines, the integrated kinetic energy distributions and mean energies of muonic atoms at the instant of their radiative  $np \rightarrow 1s$  transitions, cascade times, and so on. Hereafter, the generally accepted designations  $K\alpha$ ,  $K\beta$ ,  $K\gamma$ , and  $K\delta$  are used for  $K_i$  lines corresponding to the  $2p \rightarrow 1s$ ,  $3p \rightarrow 1s$ ,  $4p \rightarrow 1s$ , and  $5p \rightarrow 1s$  radiative transitions. Their energies are 1.90 keV, 2.25 keV, 2.37 keV, and 2.43 keV in  $\mu^-p$  atom and accordingly 2.00 keV, 2.37 keV, 2.50 keV, and 2.56 keV in  $\mu^-d$  atom.

Some of our results are compared with the available experimental data on the density dependence of the relative  $x$ -ray yields of  $K$  lines [58–61], intensity ratio of  $K\alpha$  and  $K\beta$  lines [58, 60, 61], and cascade times [10, 43, 45].

#### A. Absolute and relative $x$ -ray yields of $K$ lines

The absolute  $x$ -ray yield  $Y_i$  of the specific  $K_i$  line is determined as the intensity of this line per one formed muonic atom. Besides,  $Y_{\geq \delta}$  is a summary absolute  $x$ -ray

yield of all  $K$  lines corresponding to radiative transitions  $np \rightarrow 1s$  ( $n \geq 5$ ), and  $Y_{\text{tot}} = \sum_i Y_i$  ( $i = \alpha, \beta, \text{etc.}$ ) is a total absolute yield of all  $K$  lines.

The calculated absolute  $x$ -ray yields of  $K\alpha$ ,  $K\beta$ , and  $K\gamma$  lines as well as the summary absolute yield of  $K_{\geq\delta}$  lines and the total absolute yield  $Y_{\text{tot}}$  for  $\mu^-p$  and  $\mu^-d$  atoms are shown in Fig. 15. The calculations were performed in the relative hydrogen density range  $\varphi = 10^{-8} - 1$  at target temperature  $T = 30$  K.

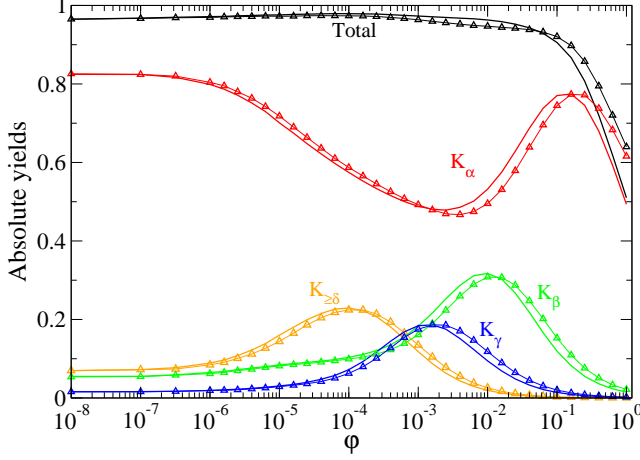


FIG. 15: (Color online) The density dependence of absolute yields for  $K\alpha$ ,  $K\beta$ ,  $K\gamma$ , and  $K_{\geq\delta}$  lines, and  $Y_{\text{tot}}$  calculated for  $\mu^-p$  (lines) and  $\mu^-d$  (lines with triangles) atoms at target temperature  $T=30$  K.

As a whole, the absolute  $K$  line yields as well as the total absolute yields have a similar dependence on the density both for  $\mu^-p$  and for  $\mu^-d$  atoms. Their density dependencies reveal a few general features discussed below.

At the lowest relative densities  $\varphi \lesssim 10^{-7}$ , the de-excitation cascade in  $\mu^-p$  and  $\mu^-d$  atoms are largely determined by the initial  $n$ - $l$  distributions and the rates of radiative transitions and muon decay. The rate of the muon decay is applied to be equal to  $\lambda_\mu = 4.54 \cdot 10^5 \text{ s}^{-1}$ , that corresponds to the free muon lifetime  $\tau_\mu = 2.2 \cdot 10^{-6} \text{ s}$ . Here the radiative transitions dominate over other processes, thus leading to the population of circular states of the muonic atom and mainly to the radiative transition  $2p \rightarrow 1s$  at the end of the cascade. At these densities the  $np$  ( $n \geq 3$ ) states are populated much weaker during the cascade mainly because of initial conditions defined in Eqs. (22) and (23). We see the corresponding picture in Fig. 15 both for  $\mu^-p$  and  $\mu^-d$  atoms. In particular, at  $\varphi = 10^{-8}$  the present cascade calculations predict for  $\mu^-p$  and  $\mu^-d$  atoms practically the same absolute yields:  $Y_\alpha = 0.825$ ,  $Y_\beta = 0.054$ ,  $Y_\gamma = 0.016$ , and  $Y_{\geq\delta} = 0.070$  (here the total absolute yield amounts to  $Y_{\text{tot}} = 0.965$ ). At this density about 3.5% of all formed muonic atoms undergo the  $\mu$ -decay: 2% of  $\mu$ -decay occur in the  $2s$  state (both above and below  $2s - 2p$  threshold) and accordingly 1.5% of muons decay in states with  $n \geq 3$ .

The absolute  $Y_\alpha$  and  $Y_{\text{tot}}$  yields calculated previously (see Fig. 6 in [12]) for muonic hydrogen at the density  $\varphi = 10^{-8}$  do not agree with the present predictions and

are equal to about 0.95 and 1, respectively. Besides, the so-called radiative mode of the arrival population of the  $2s$  state (see Eq. 21 in [31]) calculated with these absolute yields [12] is obtained to be  $\simeq 0.7\%$ , that is almost three times less than the present prediction 2%. All these differences can be explained only by the effect of initial distributions on quantum numbers  $n$  and  $l$  ( $n_i = 14$  and the  $l_i$  distribution is statistical) applied in [12].

In the wide density range from  $\varphi = 10^{-8}$  up to  $\varphi \approx 2.5 \cdot 10^{-3}$  the density dependence of the total absolute is very weak. Contrary to this, the absolute yields of individual  $K_i$  lines have a more complicated density dependence. With the increase in density above  $\varphi = 10^{-7}$  the role of collisional processes in highly excited states ( $n \geq 5$ ) is steadily enhanced, that leads to the decrease in  $K\alpha$  line yield and simultaneously to the increase in the absolute yields of the other  $K_i$  ( $i = \beta, \gamma, \text{etc.}$ ) lines, conserving the total absolute yield  $Y_{\text{tot}}$  practically unchangeable in the limit of a few percent.

The absolute  $K\alpha$  yield reach their minimum values  $Y_\alpha = 0.478$  at  $\varphi \simeq 2.5 \cdot 10^{-3}$  for  $\mu^-p$  atom and  $Y_\alpha = 0.465$  at  $\varphi \simeq 3.5 \cdot 10^{-3}$  for  $\mu^-d$  atom. At higher densities the absolute  $K\alpha$  yield rapidly grows and achieves its maximum value 0.78 at  $\varphi = 0.13$  for  $\mu^-p$  atom and at  $\varphi = 0.18$  for  $\mu^-d$  atom, respectively. The enhancement of the absolute  $K\alpha$  line yield observed in this density region is mainly explained by both the external Auger and CD  $3 \rightarrow 2$  of muonic atoms.

Further density increase leads to a significant reduction of both  $Y_\alpha$  and  $Y_{\text{tot}}$ . At  $\varphi = 1$  the present calculations predict:  $Y_\alpha = 0.493$  and  $Y_{\text{tot}} = 0.510$  (for  $\mu^-p$  atom) and  $Y_\alpha = 0.616$  and  $Y_{\text{tot}} = 0.640$  (for  $\mu^-d$  atom). Therefore, the isotopic effect predicted at the liquid hydrogen density for  $Y_\alpha$  and  $Y_{\text{tot}}$  is about 25%. It would be very useful to check these predictions in measurements of absolute  $x$ -ray yields at this density for both muonic hydrogen and muonic deuterium atoms.

A sharp decrease in the absolute yields of the  $Y_\alpha$  and  $Y_{\text{tot}}$  is explained by the formation (during the de-excitation cascade) of a muonic atom ( $\mu^-p$ ) $_{2s}$  (or ( $\mu^-d$ ) $_{2s}$ ) with kinetic energy below the  $2p$  threshold and its subsequent CD  $2s \rightarrow 1s$ . In the density region  $\varphi = 0.1 - 1$  both the population of the  $2s$  state below the  $2p$  threshold and the rate of the CD  $2s \rightarrow 1s$  in the case of the  $\mu^-p$  atom is on average about a few times more than corresponding values in the  $\mu^-d$  atom case.

In the present study the collision-induced radiative decay of the  $2s$  state below  $2p$  threshold was not considered. This process will be studied in details in a separate paper together with the other decay modes of the  $2s$  state. Note, that this process leads to the increase in  $Y_\alpha$  and correspondingly in  $Y_{\text{tot}}$ .

The density dependence of absolute  $K$  line yields ( $n \geq 3$ ) reveals quite similar behavior with the increase in density, which may be conventionally divided into three stages and correspondingly three density regions. In the first region, the absolute yields slowly increase (about two times) with the density compared to their initial values at the lowest density ( $\varphi = 10^{-8}$ ). The corresponding density regions are different for various  $K_{\geq\beta}$  lines:  $\varphi \lesssim 8 \cdot 10^{-5}$  for  $K\beta$  line,  $\varphi \lesssim 2 \cdot 10^{-5}$  for



$K\gamma$  line, and  $\varphi \lesssim 6 \cdot 10^{-6}$  for  $K\delta$  line, etc. In the second region, the absolute yields of  $K_{\geq\beta}$  lines grow very rapidly achieving their maximum values at different densities (e.g.,  $\varphi = 3 \cdot 10^{-4}$  for  $K\delta$  line,  $\varphi = 1.2 \cdot 10^{-3}$  for  $K\gamma$  line, and  $\varphi = 1.3 \cdot 10^{-2}$  for  $K\beta$  line). Finally, in the third region, the absolute yields of  $K_{\geq\beta}$  lines practically go to zero with the further density increase, excluding the  $K\beta$  line. Thus, the absolute yields of  $K_{\geq\beta}$  lines form the family of the similar curves with maxima, which values increase about two times, whereas  $n$  is decreasing.

The physical reason of the maximum formation in absolute yields of all  $K$  lines ( $K\alpha$ ,  $K\beta$ ,  $K\gamma$ , etc.) has a similar nature — the interplay between the rates of radiative transitions, from one side, and the rates of the external Auger effect and CD, from the other side. All maxima are largely formed by the increase in rates of external Auger and CD transitions from the above lying states. At the same time, the absolute yields of  $K_{\geq\beta}$  lines decrease in the third region, because the summary rate of the external Auger effect and Coulomb de-excitation from states with  $n \geq 3$  becomes comparable and even much more than the rate of the corresponding radiative  $np \rightarrow 1s$  transition.

The  $\mu^-d$  absolute yields slightly differ from  $\mu^-p$  ones at densities below  $10^{-3}$ . At higher densities the isotopic effect increases and becomes much stronger in the absolute yields of  $K\gamma$ ,  $K\beta$ , and especially  $K\alpha$  lines.

It is noteworthy, that the significant contribution to the total absolute yield comes from  $K_{\geq\delta}$  lines in a wide density range  $\varphi \lesssim 3 \cdot 10^{-3}$ . Their summary yield is comparable with  $Y\beta$  at density  $\varphi \lesssim 10^{-6}$  and even about two times more at  $\varphi \lesssim 10^{-4}$ . This result should be taken into account in the analysis of experimental data.

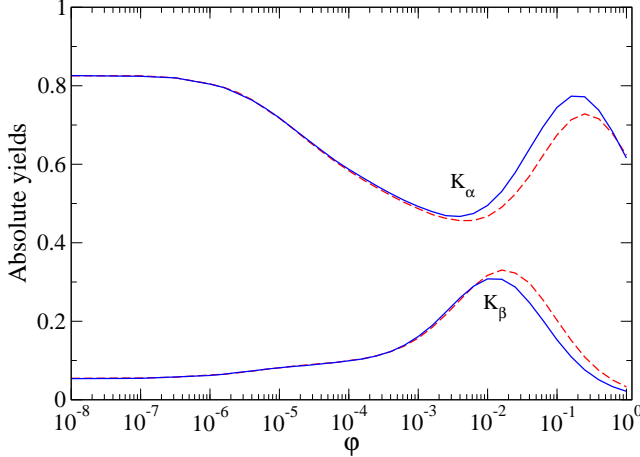


FIG. 16: (Color online) The temperature effect in the density dependence of the absolute  $x$ -ray yields for  $K\alpha$  and  $K\beta$  lines in muonic deuterium calculated at target temperature  $T=30$  K (solid lines) and  $T=300$  K (dashed lines).

The exact kinematics of binary collisions taking into account the target motion (see Eqs. (25)-(27)) is used explicitly in the present cascade model. This leads to effects, which could be observed in precision experiments produced at densities above  $\approx 10^{-2}$  and essentially different target temperature. To illustrate this effect, the absolute  $x$ -ray yields of  $K\alpha$  and  $K\beta$  lines for the  $\mu^-d$

atom were calculated at two values of the target temperature  $T = 30$  K and  $T = 300$  K (see Fig. 16). One can see, that the absolute yields of both  $K\alpha$  and  $K\beta$  lines differ essentially at the density above  $\varphi \gtrsim 10^{-2}$  with the increase in temperature from  $T = 30$  K to  $T = 300$  K.

The observed temperature effect is explained by the strong energy dependence of the CD rate shown in Figs. 11. The increase in target temperature from  $T=30$  K to  $T=300$  K and accordingly the mean kinetic energy of the target on one order of magnitude makes the process of the CD  $3 \rightarrow 2$  less effective (at a fixed density) than the radiative transition  $3p \rightarrow 1s$ . As a result, at the density above  $\varphi \approx 10^{-2}$  the absolute yields of the  $K\beta$  line calculated at  $T=300$  K increase, whereas the absolute yields of the  $K\alpha$  line decrease in comparison with their values calculated at the target temperature  $T=30$  K.

The discussed above regularities in absolute  $x$ -ray yields of different  $K$  lines should also take place in their relative yields defined by the ratio  $Y_i/Y_{\text{tot}}$ . The present results for  $\mu^-p$  and  $\mu^-d$  atoms are compared with available experimental data [58–61].

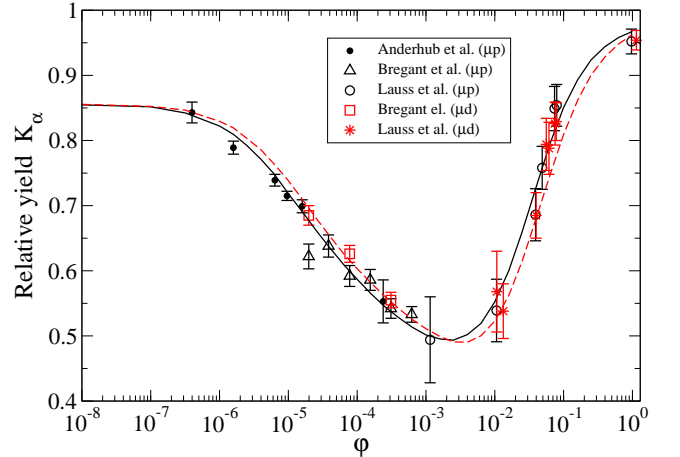


FIG. 17: (Color online) The density dependence of the relative  $K\alpha$  line  $x$ -ray yields for  $\mu^-p$  (solid line) and  $\mu^-d$  (dashed line) atoms. The experimental data are from [58–61].

The density dependence of the relative  $K\alpha$  line  $x$ -ray yields for muonic hydrogen and deuterium is shown in Fig. 17. The calculations were done at the target temperature  $T = 30$  K that corresponds to experimental conditions [60, 61]. It is noteworthy, that the temperature dependence of both absolute and relative  $x$ -ray yields is very weak at the density range below  $\varphi \approx 10^{-3}$ , where experimental data [58, 59] have been obtained. As a whole, the theoretical values of relative  $x$ -ray yields of  $K\alpha$  line are in very good agreement with experimental data [58–61], obtained in the wide density range from  $\varphi = 3.98 \times 10^{-7}$  up to 1.14 (in the case of  $\mu d$  atom). In our opinion, the observed disagreements between theoretical and experimental results for  $\mu^-p$  in a few values of density (e.g., at  $\varphi \simeq 1.6 \cdot 10^{-6}$  and  $\varphi \simeq 2 \cdot 10^{-5}$ ) can not be explained by the possible theoretical uncertainties in the present study. In particular, the experimental value of the relative  $K\alpha$  line  $x$ -ray yield at  $\varphi \simeq 2 \cdot 10^{-5}$  (0.622 [59]) is obviously much lesser than the value 0.699 obtained in



[58] at a very close value of density  $\varphi \simeq 1.6 \cdot 10^{-5}$ , which, in turn, is in excellent agreement with the present result 0.690.

The comparison of the relative  $x$ -ray yields of  $K\alpha$  line calculated for muonic hydrogen and deuterium reveals the isotopic effect observed above in absolute yields (see Fig. 15). At density below  $\sim 10^{-3}$ , the relative yields of  $K\alpha$  line in the case of  $\mu^-d$  atoms are slightly larger than for  $\mu^-p$  atom case, that is in correspondence with experimental data [59]. At densities higher than  $\varphi \approx 3 \cdot 10^{-3}$  we observe the opposite picture, viz. the relative  $x$ -ray yields of  $K\alpha$  line in the case of  $\mu^-d$  atoms are lesser than in  $\mu^-p$  atom case. Unfortunately, the accuracy of experimental data [60, 61] does not allow to confirm our predictions in this density range. Besides, there are not any experimental data in a very interesting density range  $0.1 \lesssim \varphi < 1$ .

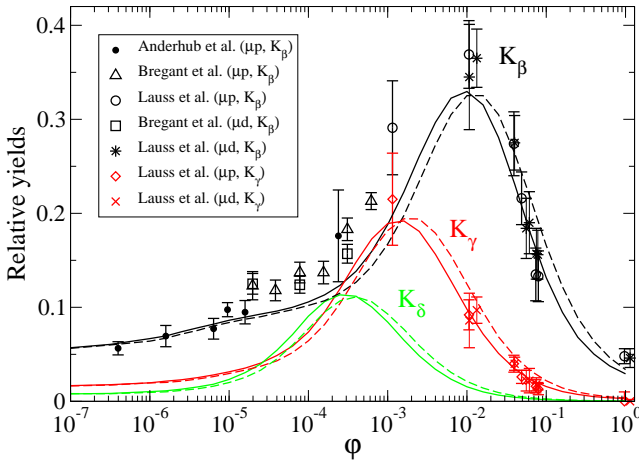


FIG. 18: (Color online) The density dependence of relative  $x$ -ray yields of  $K\beta$ ,  $K\gamma$ , and  $K\delta$  lines in muonic hydrogen (solid lines) and deuterium (dashed lines). The experimental data are from [58–61].

In Fig. 18 the density dependencies of the relative  $x$ -ray yields of  $K\beta$ ,  $K\gamma$ , and  $K\delta$  lines from muonic hydrogen and deuterium are shown. The calculations were done at target temperature  $T = 30$  K. The agreement between the present theoretical results and experimental data [58–61] is rather good practically at all densities under consideration. In our opinion, the observable disagreements between the theoretical and experimental relative yields of the  $K\beta$  line in the density range  $\varphi \approx 3 \cdot 10^{-5} - 3 \cdot 10^{-3}$  may be explained only by experimental reasons: the separation of  $K\beta$ ,  $K\gamma$ , and  $K(\geq \delta)$  lines, the efficiency of their registration and so on. It would be very useful to check out these predictions by remeasuring relative yields in this density range with a much better accuracy.

Figure 19 shows our results for the density dependence of  $Y_\alpha/Y_\beta$  ratios for muonic hydrogen,  $R_{\mu p}$ , and deuterium,  $R_{\mu d}$ , as well as their differences,  $(R_{\mu p} - R_{\mu d})$ . This difference serves as a direct demonstration of the isotopic effect. Comparing  $R_{\mu p}$  with  $R_{\mu d}$  at densities below  $10^{-2}$ , one can see that the ratio  $R_{\mu d}$  is slightly larger than the  $\mu p$  one. At densities  $5 \cdot 10^{-2} \lesssim \varphi \lesssim 0.8 \cdot 10^{-2}$  we predict the density dependence of  $R_{\mu d}$ , which is systematically lesser than experimental data [61]. However, at

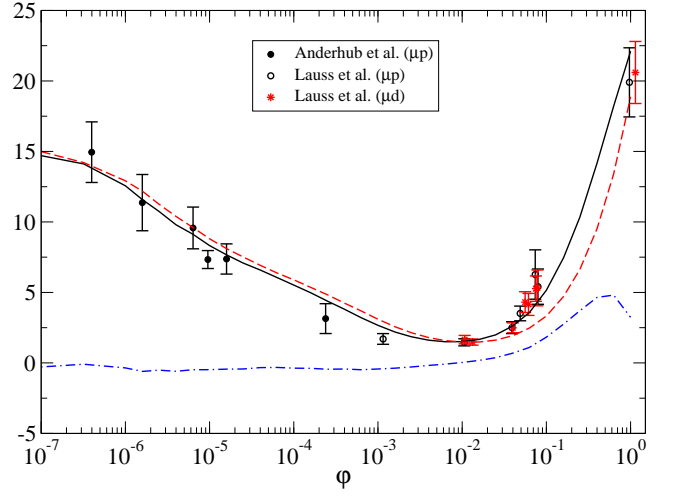


FIG. 19: (Color online) The density dependence of the  $Y_\alpha/Y_\beta$  ratio for muonic hydrogen (solid line) and deuterium (dashed line), as well as their differences (dashed-dotted line). The experimental data are from [58, 60, 61].

liquid hydrogen density both theoretical prediction and experimental result are in an excellent agreement.

Our results have a natural explanation. In the case of the muonic deuterium the rate of the  $CD\ 3 \rightarrow 2$  is suppressed more than one order of magnitude in comparison with the muonic hydrogen (see Fig. 11). This leads to the increase in  $Y_\beta$  and correspondingly to the decrease in  $Y_\alpha$  in the case of the  $(\mu^-d)$  atom as compared with  $(\mu^-p)$  one in the density range above  $\approx 10^{-2}$ . It is noteworthy, that differences  $(R_{\mu p} - R_{\mu d})$  grow at densities above  $10^{-2}$  and reach their maximum at the density about  $7 \cdot 10^{-1}$ .

The present study shows that additional measurements of the yields with much better accuracy in the density region between  $3 \cdot 10^{-5}$  and  $3 \cdot 10^{-3}$  as well as at densities above  $\approx 5 \cdot 10^{-2}$  are extremely important.

## B. Kinetic energy distribution

In addition to the natural line width and the resolution of the apparatus (response function), the experimental profile (line shape) of the  $np \rightarrow 1s$   $x$ -ray lines in muonic and hadronic hydrogen atoms is determined by the Doppler broadening due to the motion of the exotic atom at the instant of its radiative transition. Therefore, the kinetic energy of exotic atoms, resulting from the complex interplay of various cascade processes, preceding the  $x$ -ray emission, is needed in the analysis of precision spectroscopic experiments. The kinetic energy distribution of the exotic atom changes during the de-excitation cascade and very sensitive to the rates of collisional processes involved in the atomic cascade. Thus, it may be considered as one of the refined tests of both the theoretical approaches, applied to describe various scattering processes, and the models of kinetics of the atomic cascade.

The calculations of the kinetic energy distributions of exotic atoms at the time of their radiative  $np \rightarrow 1s$  transitions in muonic and pionic hydrogen atoms have been

performed previously (e.g., see [52, 53]), to improve the description of the Doppler broadening in measured profiles of  $x$ -ray lines: for the  $\mu^-p$  atom [13, 14] and for the  $\pi^-p$  atom (see [15] and references therein).

In order to take into account the  $K_i$  line broadening, which originates from the motion of exotic atoms, the probability density  $\omega_{K_i}(E; \varphi, T)$  of their energy distribution should be calculated for the given target density and temperature and be used in the analysis of the experimental line shape. Here we represent the distribution function of the probability,

$$I_{K_i}(E; \varphi, T) = \int_0^E \omega_{K_i}(E'; \varphi, T) dE', \quad (28)$$

that the muonic atom has a kinetic energy less than  $E$  at the instant of the  $K_i$  line emission.

The energy distribution at low  $n$  can be determined by measuring the Doppler broadening of  $K$   $x$ -ray lines, since high-energy components lead to a significant Doppler broadening, which is especially pronounced for  $K\alpha$  line. The calculated distribution functions  $I_{K\alpha}(E; \varphi, T)$  of  $\mu^-p$  and  $\mu^-d$  atoms are shown in Figs. 20 and 21, respectively. The calculations were performed at target temperature  $T = 300$  K and a few values of the relative target density:  $\varphi = 10^{-8}, 10^{-5}, 10^{-3}, 10^{-2}$ , and  $10^{-1}$ . The energy distributions of muonic atoms in Figs. 20 and 21 calculated at a relative density  $\varphi = 10^{-8}$  coincide with the initial energy distribution of muonic atoms at the time of their formation (see Eq. (24)). Here we will use the arbitrary choice of 2 eV as the boundary between low-energy and high-energy fractions in the energy distributions of muonic atoms.

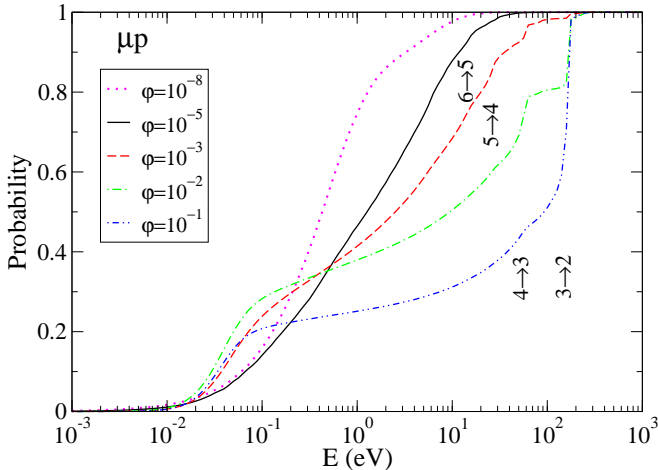


FIG. 20: (Color online) The kinetic energy distribution of the  $\mu^-p$  atom at the instant of the radiative transition  $2p \rightarrow 1s$  calculated at various relative target densities  $\varphi$  (target temperature  $T = 300$  K). The kinetic energies, which muonic atoms acquire after CD transitions  $n \rightarrow n'$ , are shown by arrows.

With the increase in density, the role of Coulomb transitions grows, and the energy distribution of muonic atoms becomes more energetic. In particular, in the case of muonic hydrogen, as shown in Fig. 20, the low-energy fraction of the muonic hydrogen with kinetic energy less

than 2 eV decreases drastically with the relative density increase from  $\varphi = 10^{-8}$  to  $\varphi = 10^{-1}$ . The probability of this fraction is about 0.87 at density  $\simeq 10^{-8}$  (in correspondence with Eq. (24)) and strongly decreases with the density growth to: about 0.58 at  $\varphi = 10^{-5}$ , 0.48 at  $\varphi = 10^{-3}$ , 0.41 at  $\varphi = 10^{-2}$ , and 0.26 at  $\varphi = 10^{-1}$ . At the same time, the probability of the high-energy fraction with kinetic energy  $E > 2$  eV becomes much more pronounced with the increase in density and reveals noticeable contributions of preceding Coulomb transitions, e.g.,  $7 \rightarrow 6$ ,  $6 \rightarrow 5$ ,  $5 \rightarrow 4$ ,  $4 \rightarrow 3$ , and  $3 \rightarrow 2$ .

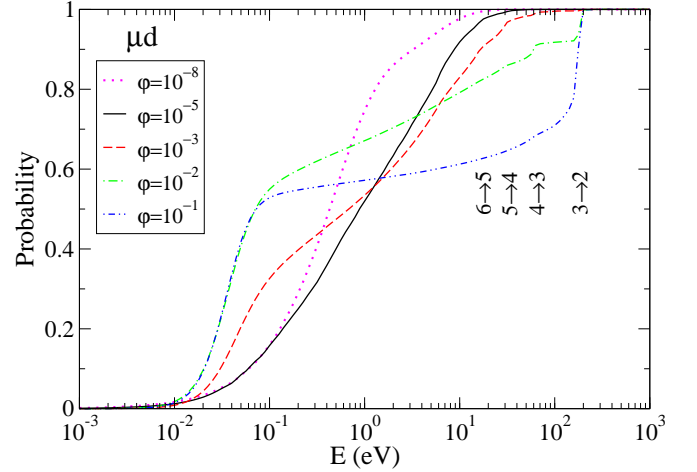


FIG. 21: (Color online) The same as in Fig. 20 for  $\mu^-d$  atom at the instant of the radiative  $2p \rightarrow 1s$  transition.

In the case of the muonic deuterium (see Fig. 21), the evolution of the kinetic energy distribution (in the same density range) is quite different. Here, the present cascade calculations predict practically the similar change of the probability of the low-energy fraction from 0.87 to 0.64 in the density range  $\varphi = 10^{-8} - 10^{-5}$ . However, at higher densities ( $\varphi > 10^{-5}$ ), the contributions of Coulomb transitions  $6 \rightarrow 5$ ,  $5 \rightarrow 4$ ,  $4 \rightarrow 3$ , and  $3 \rightarrow 2$  are much weaker in comparison with the muonic hydrogen case. As a result, the probability of the low-energy fraction is about 0.60 at  $\varphi = 10^{-3}$  and  $\varphi = 10^{-1}$  and constitutes even 0.70 at  $\varphi = 10^{-2}$ . The strong isotopic effect observed in the kinetic energy distributions of muonic hydrogen and deuterium atoms is mainly explained by the strong isotopic effect in the cross sections of Coulomb de-excitation discussed above in the previous section.

As shown in Figs. 20 and 21, the calculated kinetic energy distributions have distinctive high-energy components arising from various Coulomb transitions with  $\Delta n \geq 1$ , preceding the radiative de-excitation  $2p \rightarrow 1s$ . In particular, the contributions of Coulomb de-excitations  $6 \rightarrow 5$  (at 14.6 eV for  $\mu^-p$  and 15.8 eV for  $\mu^-d$ ),  $5 \rightarrow 4$  (at 26.9 eV for  $\mu^-p$  and 29.1 eV for  $\mu^-d$ ), and  $4 \rightarrow 3$  (at 58.2 eV for  $\mu^-p$  and 62.9 eV for  $\mu^-d$ ) are revealed in the wide density range  $\varphi > 10^{-5}$ . They survive until the de-excitation of muonic atoms to the  $2p$  state due to successive Auger and radiative transitions between above lying states. With the density increase, the contributions of individual CD transitions become much less pronounced because of the deceleration

through the elastic scattering and Stark mixing. Nevertheless, the contribution of the CD transition  $4 \rightarrow 3$  is even noticeable at target density  $10^{-1}$ . It is noteworthy, that the contribution of the CD transition  $3 \rightarrow 2$  (at 166.2 eV for  $\mu^-p$  and 179.9 eV for  $\mu^-d$ ) with the density increase from  $\varphi = 10^{-3}$  to  $\varphi = 10^{-1}$  grows from a few percent up to 55% for  $(\mu^-p)_{2p}$  and only to about 30% for  $(\mu^-d)_{2p}$ .

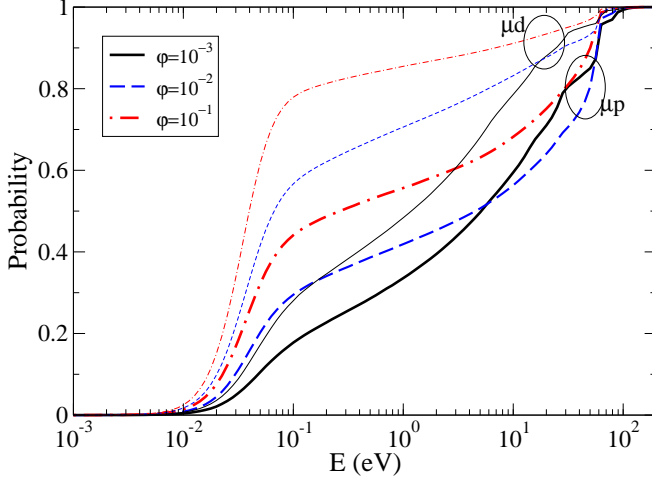


FIG. 22: (Color online) The kinetic energy distributions of  $\mu^-p$  (thick lines) and  $\mu^-d$  (thin lines) atoms at the instant of their radiative  $3p \rightarrow 1s$  transition calculated at a few values of the relative target density  $\varphi$  (target temperature  $T = 300$  K).

The energy distributions of  $\mu^-p$  and  $\mu^-d$  atoms, calculated at the instant of their radiative  $3p \rightarrow 1s$  transition are shown in Fig. 22. The calculations were performed for three values of the relative target density:  $\varphi = 0.001$ ,  $\varphi = 0.01$ , and  $\varphi = 0.1$ . The target temperature is chosen to be  $T = 300$  K.

Here the energy distributions of  $\mu^-p$  and  $\mu^-d$  atoms calculated at the same density differ significantly. The energy distributions of  $(\mu^-p)_{3p}$  contain quite strong contributions from preceding  $(5 \rightarrow 4)$ ,  $(5 \rightarrow 3)$ , and especially  $(4 \rightarrow 3)$  CD. For example, the Coulomb de-excitation  $(4 \rightarrow 3)$  at  $\varphi = 0.01$  makes up to about 25% in the case of the muonic hydrogen, whereas in the case of the muonic deuterium it contributes only about 7%. The predicted probabilities of low-energy fractions ( $E \leq 2$  eV) at densities  $\varphi = 0.001$ ,  $\varphi = 0.01$ , and  $\varphi = 0.1$  have also a very strong differences: 40%, 47%, and 58% for  $(\mu^-p)_{3p}$  and correspondingly 55%, 74%, and 87% for  $(\mu^-d)_{3p}$ .

The strong isotopic effect discovered in the present study in the scattering and the kinetics of the atomic cascade of muonic hydrogen and deuterium atoms allows to explain the true reason, why the kinetic energy distribution of the  $(\pi^-p)_{3p}$  (at the instant of the radiative  $(3p \rightarrow 1s)$  transition), scaled to the  $(\pi^-d)_{3p}$  case, is unable adequately to reproduce the Doppler induced width [39]. There are also other reasons that are not the subject of this study, which does not allow to justify the procedure of the scaling of the kinetic energy distribution. In the case of the pionic deuterium the rates of the absorption from  $ns$  states and collision-induced ab-

sorption [33] as well as the rates of radiative transitions are larger than in the case of pionic hydrogen. As a result of these processes, the probability of the CD in the case of the pionic deuterium, in addition to the isotopic effect discussed above, becomes also lesser during the de-excitation cascade than in the pionic hydrogen case.

The acceleration of muonic atoms during the cascade is also illustrated in Fig. 23. Here, the density dependence of the mean kinetic energy

$$\overline{E}_{K_i}(\varphi, T) = \int_0^\infty E' \omega_{K_i}(E'; \varphi, T) dE' \quad (29)$$

of  $\mu^-p$  and  $\mu^-d$  atoms, calculated at the instant of their radiative transitions  $2p \rightarrow 1s$  and  $3p \rightarrow 1s$ , is shown. The calculations were performed in the relative density range from  $10^{-5}$  up to 1 at room temperature  $T = 300$  K. At a given temperature the mean kinetic energy of the

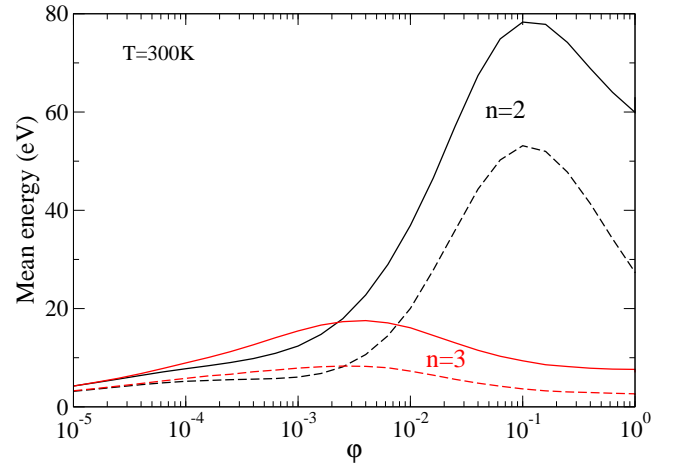


FIG. 23: (Color online) The density dependence of the mean kinetic energy of  $\mu^-p$  (solid lines) and  $\mu^-d$  (dashed lines) atoms at the instant of their radiative transitions  $2p \rightarrow 1s$  and  $3p \rightarrow 1s$ .

$\mu^-d$  at the instant of  $2p \rightarrow 1s$  and  $3p \rightarrow 1s$  radiative transitions is always less than the mean kinetic energy of the  $\mu^-p$  at all densities under considerations, excluding the lowest density  $10^{-8}$ , at which the mean energy of both muonic hydrogen and deuterium is equal to 1.32 eV and is in perfect agreement with the experimental value  $1.3 \pm 0.8$  eV [10].

In the considered density range the mean kinetic energies of  $\mu^-p$  and  $\mu^-d$  atoms increase steadily from a few electron volts at density  $10^{-5}$  and reach their maxima (respectively at  $3 \cdot 10^{-3}$  for  $K\beta$  lines and at 0.12 for  $K\alpha$  lines of  $\mu^-p$  and  $\mu^-d$  atoms).

In particular, at the density  $10^{-5}$  the mean kinetic energies of both muonic hydrogen and deuterium at the instant of their emission of  $K\alpha$  and  $K\beta$  lines are the same and equal to 4.28 and 3.30 eV, respectively. At higher densities, the mean energy of the  $(\mu^-p)_{3p}$  grows and at the density  $3 \cdot 10^{-3}$  reaches the maximum value  $\simeq 17$  eV and about a factor two less, viz.  $\simeq 8$  eV, in the case of the  $(\mu^-d)_{3p}$ .

The most significant increase in mean energy is revealed for muonic atoms in the  $2p$  state during the emission of the  $K\alpha$  line. Here, in the density range from

$3 \cdot 10^{-3}$  to 0.12 the mean energy of muonic hydrogen and deuterium rapidly grows from 17 eV up to 78 eV for  $\mu^-p$  and from 8 eV up to 53 eV for  $\mu^-d$  atoms, respectively. At the liquid hydrogen density the mean kinetic energies of  $\mu^-p$  and  $\mu^-d$  atoms before radiative  $2p \rightarrow 1s$  transition also have a large difference. In our calculations we obtain 60 eV and 24 eV for  $(\mu^-p)_{2p}$  and  $(\mu^-d)_{2p}$ , respectively. This isotopic effect is mainly explained by the observed isotopic effect in CD rates of  $4 \rightarrow 3$  and  $3 \rightarrow 2$  transitions in  $\mu^-p$  and  $\mu^-d$  atoms (e.g., see Figs. 11 and 12, as well as Figs. 20-22). It is noteworthy, that the density dependence of the mean kinetic energy calculated for  $\mu^-p$  and  $\mu^-d$  atoms is in qualitative agreement with the data [9].

### C. Cascade time

The mean time interval between the formation of the muonic atom and its arrival in the  $1s$  state is determined by the cascade time. In the present study we calculate the so-called prompt cascade time which does not include the life time of the  $2s$  state at kinetic energy both above and below  $2p$  threshold. To find the prompt cascade time,  $\tau_{\text{casc}}$ , at low target densities  $\varphi \lesssim 10^{-4}$ , we calculate the probability of the  $\mu$  decay,  $p_\mu$ , during the de-excitation cascade (beyond the  $2s$  state)

$$p_\mu = 1 - e^{-\tau_{\text{casc}}/\tau_\mu}. \quad (30)$$

Here the probability  $p_\mu$  is defined as the ratio of the number of the  $\mu$  decay to the total number of formed muonic atoms. Then the cascade time is given by

$$\tau_{\text{casc}} = \tau_\mu \ln \frac{1}{1 - p_\mu}. \quad (31)$$

TABLE II: The cascade times  $\tau_{\text{casc}}$  of  $\mu p$  and  $\mu d$  atoms at various target pressures  $p$  ( $T = 293$  K).

$p$ (hPa)	$\tau_{\text{casc}}^{\mu p}$ (ns)			$\tau_{\text{casc}}^{\mu d}$ (ns)		
	Theory	Exp.	Ref.	Theory	Exp.	Ref.
$8.55 \cdot 10^{-3}$	37.9			34.3		
0.6	27.7	$26 \pm 5^a$	[43]	28.1		
		$39 \pm 5^b$	[43]			
1	24.1	$27.7 \pm 3^a$	[45]	27.4	$28.6 \pm 1.9^a$	[45]
		$25.0 \pm 1.5^b$	[45]		$31.6 \pm 1.7^b$	[45]
		$28 \pm 8$	[10]			
4	15.5	$26 \pm 6$	[10]	17.8		
16	8.3	$11 \pm 5$	[10]	8.9		

<sup>a</sup>From  $K\alpha$  time spectrum

<sup>b</sup>From  $K \geq \gamma$  time spectrum

At relative target density  $\varphi = 10^{-8}$  (target pressure about  $8.55 \cdot 10^{-3}$  hPa), where the de-excitation cascade is purely radiative, we predict  $\tau_{\text{casc}}^{\mu p} = 37.9$  ns and  $\tau_{\text{casc}}^{\mu d} = 34.3$  ns. The observed  $\approx 10\%$  difference is explained by the dependence of the radiative transition rate on the reduced mass of the muonic atom. We remind, that the

reduced mass in the muonic deuterium is about 5% more than in the muonic hydrogen case.

At higher density the role of collisional processes increases, that essentially affects the cascade time. The cascade time decreases with the increase in target density owing to collisional processes. In our study, at a fixed density, the rates of collisional processes in the muonic hydrogen case are larger than in the muonic deuterium one (e.g., see Figs. 8 -12). Therefore, the cascade time in muonic hydrogen should become less than in muonic deuterium with the increase in density.

To illustrate this isotopic effect, in Table I we represent cascade times in  $\mu p$  and  $\mu d$  atoms. The calculations were performed at a few values of the target pressure  $p = 8.55 \cdot 10^{-3}, 0.6, 1, 4$ , and 16 hPa and temperature  $T = 293$  K, corresponding to experimental conditions[10, 43, 45]. The experimental data [10] were obtained in  $(\mu^-p)_{1s}$  diffusion experiments, whereas the measured cascade times [43, 45] were extracted by fitting time spectra of the muonic hydrogen/deuterium  $K \geq \gamma$  and  $K\alpha$  x-rays. These experimental data are also given in Table 1 for comparison with the present results.

As a whole, the cascade times calculated for  $\mu p$  and  $\mu d$  atoms are in very good agreement with experimental data [10, 43, 45]. In particular, the experimental fact[45] that the cascade time in  $\mu d$  is about 10% more than in  $\mu p$  at a given pressure 1 hPa is in correspondence with the present theoretical calculations of collisional cross sections used in the kinetics of the atomic cascade.

## IV. CONCLUSION

The fully quantum-mechanical description of the scattering processes – elastic scattering, Stark mixing, and CD – has been done in the framework of the close-coupling approach for collisions of excited  $\mu^-p$  and  $\mu^-d$  atoms correspondingly with an ordinary hydrogen and deuterium atoms in their ground state. The energy shifts between  $ns$  and  $nl$  states ( $n \geq 2$ ,  $l \geq 1$ ), mainly due to electron vacuum polarization, have been explicitly taken into account in the scattering problem for both muonic hydrogen and deuterium atoms. The threshold behavior of all cross sections was treated in a proper way. The explicit analytic expression for the matrix of interaction potentials has been obtained without any additional approximations. The propagator matrix method [31] has been used to calculate the scattering matrix defined in the subspace of the open channels.

The influence of the extension of the basis set (by including the closed channels) on the partial-wave and total cross sections of the elastic scattering, Stark transitions, and Coulomb de-excitation has been studied. It was found, that the convergence of the close-coupling approach in the scattering problem under consideration is achieved very slowly due to a strong coupling between the closed and open channels. To our study, the closed channel effect is especially significant in the low-energy scattering of exotic atoms in low-lying excited states ( $n = 2 - 5$ ). Here the convergence of the cross sections of different processes has been achieved by applying the

extended basis set including all the exotic atom states with the principal quantum number up to  $n_{\max} = 20$ . The cross sections of elastic scattering, Stark transitions and Coulomb de-excitation have been calculated reliably both above and below  $ns - np$  thresholds.

The systematic calculations of the integrated and differential cross sections of elastic scattering, Stark transitions, and CD have been performed for the  $\mu^-p$  and  $\mu^-d$  atoms in excited states ( $n \geq 2$ ) and kinetic energies from 0.001 eV up to  $E_{\max}$  needed for the detailed study of the kinetics of the atomic cascade. All the cross sections have been calculated by applying the extended basis, which includes all open and closed channels associated with the exotic atom states with the principal quantum number up to  $n_{\max} = 20$ .

The isotopic effect in the scattering of excited  $\mu^-p$  and  $\mu^-d$  atoms has been revealed. At all collision energies the cross sections of elastic scattering and Stark transitions in the case of the  $(\mu^-d)_n + D$  scattering are about (10-15)% more than in the  $(\mu^-p)_n + H$  one. In contrast, a much stronger isotopic effect has been discovered in the cross sections of Coulomb de-excitation. For a given  $n$  and fixed  $\Delta n = n - n'$  the cross sections of the CD ( $n \rightarrow n' \leq n - 1$ ) in the case of the  $\mu^-d$  are, as a rule, less than in the case of the  $\mu^-p$ . This difference grows essentially with the decrease in  $n$  and the increase in  $\Delta n$ .

The isotopic effect discovered in both cross sections and the rates of the CD allow to predict a similar effect in the pionic deuterium and especially in the muonic tritium. This effect should lead to a very strong weakening of the high-energy components in the energy spectrum of the pionic deuterium and even much stronger in the case of the muonic tritium compared to the pionic and muonic hydrogen atoms, respectively. In particular, the predicted isotopic effect allows for the first time to explain the significant suppression of the contributions of high-energy components originating from CD transitions ( $4 \rightarrow 3$ ) and ( $5 \rightarrow 3$ ) in shift/width experiments [39] with the pionic deuterium.

The kinetics of the atomic cascade has been investigated for both  $\mu^-p$  and  $\mu^-d$  atoms within the new version of the cascade model, which has a number of significant improvements over the previous cascade models:

- The new results of the fully quantum-mechanical calculations of differential and integrated cross sections for collisional processes;
- The distributions of exotic atoms in quantum numbers  $n, l$  and the kinetic energy at the instant of their formation;
- The thermal motion of the target and the exact kinematics of binary collisions.

The cascade calculations in the muonic hydrogen and deuterium have been done in the wide density range covering 8 orders of magnitude from  $10^{-8}$  up to  $1.14$  (in the units of the liquid hydrogen density,  $N_{LHD} = 4.25 \cdot 10^{22}$  atom/cm<sup>3</sup>). A number of different characteristics of the atomic cascade have been calculated: absolute and relative  $x$  ray yields, kinetic energy distributions, and cascade times.

The main regularities revealed in the density dependence of the absolute  $x$ -ray yields of different  $K$  lines

have been discussed. The present cascade calculations predict practically the same absolute yields of all  $K$  lines for both  $\mu^-p$  and  $\mu^-d$  atoms at  $\varphi \lesssim 3 \cdot 10^{-7}$ . In the density range  $3 \cdot 10^{-7} < \varphi \lesssim 3 \cdot 10^{-3}$  the absolute yields in the case of the  $\mu^-d$  atom slightly differ from the case of the  $\mu^-p$  atom. At higher densities the isotopic effect becomes much stronger in absolute yields of  $K\gamma$ ,  $K\beta$ , and especially  $K\alpha$  lines.

The calculated relative yields in the muonic hydrogen and deuterium are in good agreement with the experimental data [58–61] practically at all densities. The observable disagreements between the theoretical and experimental relative yields of the  $K\beta$  line in the density range  $\varphi \approx 3 \cdot 10^{-5} - 3 \cdot 10^{-3}$  may be explained only by experimental reasons: the separation of  $K\beta$ ,  $K\gamma$ , and  $K(\geq \delta)$  lines, the efficiency of their registration, and so on. In our opinion, additional measurements with much better accuracy and statistics in the density region between  $3 \cdot 10^{-5}$  and  $3 \cdot 10^{-3}$  as well as at densities above  $\approx 5 \cdot 10^{-2}$  are extremely desirable. In addition to the analysis of experimental data it is necessary to include other lines ( $K\gamma$  and  $K(\geq \delta)$ ) using our predictions of their absolute yields.

The calculated kinetic energy distributions of the muonic hydrogen and deuterium demonstrate a strong isotopic effect, which is mainly explained by the strong suppression of the cross sections of the preceding Coulomb de-excitation in the muonic deuterium in comparison with the muonic hydrogen. The calculated density dependence of the mean kinetic energy of  $\mu^-p$  and  $\mu^-d$  atoms (at the instant of their radiative ( $2p \rightarrow 1s$ ) and ( $3p \rightarrow 1s$ ) transitions) is in qualitative agreement with experimental data [9]. At all densities (above  $10^{-5}$ ) the mean kinetic energy of the  $\mu^-d$  atom is always less than the mean kinetic energy of the  $\mu^-p$  atom. The predicted density dependence of the mean kinetic energy of  $\mu^-p$  and  $\mu^-d$  atoms (at the instant of their radiative ( $2p \rightarrow 1s$ ) and ( $3p \rightarrow 1s$ ) transitions) can be used to choose optimal experimental conditions for experiments similar to [9, 13] as well as to improve the quality of the analysis of experimental data.

The isotopic effect in both cross sections and the rates of the CD allows to predict a similar effect in the pionic deuterium and the muonic tritium. In particular, this effect should lead to a strong weakening of the high-energy components in the energy spectrum of the pionic deuterium and especially in the case of the muonic tritium compared to the pionic and muonic hydrogen atoms and could be observed in experiments. Besides, the predicted isotopic effect allows for the first time to explain the significant suppression of the contributions of high-energy components originating from CD transitions ( $4 \rightarrow 3$ ) and ( $5 \rightarrow 3$ ) in shift/width experiments [39] with the pionic deuterium.

The cascade times calculated for the  $\mu^-p$  and  $\mu^-d$  atoms at low target densities  $\varphi \lesssim 10^{-4}$  are in very good agreement with available experimental data [10, 43, 45].

We conclude that the present study demonstrates the overall reliability of the theoretical approach used for the description of the scattering processes of the excited muonic hydrogen and deuterium with ordinary hydrogen

isotope atoms and a very good understanding of their kinetics. The obtained results serve a good foundation to apply the current theory for the realistic study of hadronic hydrogen atoms.

## V. ACKNOWLEDGMENTS

The authors thank Detlev Gotta and Randolph Pohl who had drawn their attention to the importance of the problem and e-mail correspondence regarding some aspects of this work.

## Appendix A: Potential matrix

Here we present the derivation of the explicit analytic form for the matrix elements (11) of the interaction potential  $V(\mathbf{R}, \boldsymbol{\rho})$ , which is the result of averaging the four-body interaction potential  $V(\mathbf{r}, \boldsymbol{\rho}, \mathbf{R})$  over the ground state wave function of hydrogen atom,  $\frac{1}{\sqrt{4\pi}}R_{1s}(r)$ :

$$V(\mathbf{R}, \boldsymbol{\rho}) = \frac{1}{4\pi} \int_0^\infty dr R_{1s}^2(r) V(\mathbf{r}, \boldsymbol{\rho}, \mathbf{R}). \quad (\text{A1})$$

The interaction potential,  $V(\mathbf{r}, \boldsymbol{\rho}, \mathbf{R})$ , includes the two-body Coulomb interactions between the particles from two colliding subsystems:

$$V(\mathbf{r}, \boldsymbol{\rho}, \mathbf{R}) = V_{ab} + V_{\mu b} + V_{ae} + V_{\mu e}, \quad (\text{A2})$$

where

$$V_{ab} = |\mathbf{R} + \nu \boldsymbol{\rho} - \nu_e \mathbf{r}|^{-1}, \quad (\text{A3})$$

$$V_{\mu b} = -|\mathbf{R} - \xi \boldsymbol{\rho} - \nu_e \mathbf{r}|^{-1}, \quad (\text{A4})$$

$$V_{\mu e} = |\mathbf{R} - \xi \boldsymbol{\rho} + \xi_e \mathbf{r}|^{-1}, \quad (\text{A5})$$

$$V_{ae} = -|\mathbf{R} + \nu \boldsymbol{\rho} + \xi_e \mathbf{r}|^{-1}. \quad (\text{A6})$$

Here the following notations are used:

$$\nu = m_\mu / (m_\mu + m_a), \quad \xi = 1 - \nu, \quad (\text{A7})$$

$$\nu_e = m_e / (m_e + m_b), \quad \xi_e = 1 - \nu_e, \quad (\text{A8})$$

( $m_a, m_b, m_\mu$  and  $m_e$  are the masses of hydrogen isotopes, muon and electron, respectively).

Averaging in Eq. (A1) results in

$$V(\mathbf{R}, \boldsymbol{\rho}) = \frac{1}{\xi_e} \{U_{\nu, \xi_e}(\mathbf{R}, \boldsymbol{\rho}) - U_{-\xi, \xi_e}(\mathbf{R}, \boldsymbol{\rho})\} - \frac{1}{\nu_e} \{U_{\nu, \nu_e}(\mathbf{R}, \boldsymbol{\rho}) - U_{-\xi, \xi_e}(\mathbf{R}, \boldsymbol{\rho})\}, \quad (\text{A9})$$

where

$$U_{\alpha, \beta}(\mathbf{R}, \boldsymbol{\rho}) = \left(1 + \frac{\beta}{|\mathbf{R} + \alpha \boldsymbol{\rho}|}\right) e^{-\frac{2|\mathbf{R} + \alpha \boldsymbol{\rho}|}{\beta}} \equiv \beta \lim_{x \rightarrow 1} \left(1 - \frac{1}{2} \frac{\partial}{\partial x}\right) \frac{e^{-\frac{2x|\mathbf{R} + \alpha \boldsymbol{\rho}|}{\beta}}}{|\mathbf{R} + \alpha \boldsymbol{\rho}|}. \quad (\text{A10})$$

This representation of  $U_{\alpha, \beta}(\mathbf{R}, \boldsymbol{\rho})$  allows to apply the addition theorem for the spherical Bessel functions [62]:

$$\frac{e^{-\lambda|\mathbf{R}_1 + \mathbf{r}_1|}}{|\mathbf{R}_1 + \mathbf{r}_1|} = \frac{4\pi}{\sqrt{R_1 r_1}} \sum_{t\tau} (-1)^t Y_{t\tau}^*(\hat{\mathbf{R}}_1) Y_{t\tau}(\hat{\mathbf{r}}_1) \left\{ K_{t+1/2}(\lambda R_1) I_{t+1/2}(\lambda r_1) |_{r_1 < R_1} + I_{t+1/2}(\lambda R_1) K_{t+1/2}(\lambda r_1) |_{r_1 > R_1} \right\}, \quad (\text{A11})$$

where  $I_p(x)$  and  $K_p(x)$  are the modified spherical Bessel functions of the first and third kind, respectively.

The matrix element of interaction  $W_{n'l'L', nL}^{Jp}(R)$  between the asymptotic initial ( $nL; J$ ) and final ( $n'l'L'; J$ ) channels is defined by

$$W_{n'l'L', nL}^{Jp}(R) = \int d\boldsymbol{\rho} d\hat{\mathbf{R}} R_{nL}(\rho) R_{n'l'}(\rho) \times \mathcal{Y}_{lL}^{JM}(\hat{\boldsymbol{\rho}}, \hat{\mathbf{R}}) V(\boldsymbol{\rho}, \mathbf{R}) \mathcal{Y}_{l'L'}^{*JM}(\hat{\boldsymbol{\rho}}, \hat{\mathbf{R}}), \quad (\text{A12})$$

where the radial hydrogen-like wave functions are given explicitly by formulas:

$$R_{nL}(\rho) = N_{nL} \left(\frac{2\rho}{na}\right)^L \exp(-\rho/na) \sum_{q=0}^{n-L-1} S_q(n, L) \left(\frac{2\rho}{na}\right)^q \quad (\text{A13})$$

( $a$  is the Bohr' radius of the atom) with

$$N_{nL} = \left(\frac{2}{na}\right)^{3/2} \left[ \frac{(n+L)!(n-L-1)!}{2n} \right]^{1/2}, \quad (\text{A14})$$

and

$$S_q(n, L) = (-)^q \frac{1}{q!(n-L-1-q)!(2L+1+q)!}. \quad (\text{A15})$$

Furthermore, by substituting the Eqs.(A9)-(A11) and (A13)-(A15) into Eq.(A12) one can integrate over the angular variables ( $\hat{\mathbf{R}}, \hat{\boldsymbol{\rho}}$ ). Finally, applying the angular momentum algebra and integrating over  $\rho$ , one obtains:

$$W_{nL, n'l'L'}^{Jp}(R) = (-1)^{J+l+l'} i^{l'+L'-l-L} \sqrt{\hat{l}\hat{l}'\hat{L}\hat{L}'} \sum_{t=0}^{t_{\max}} (l0l'0|t0)(L0L'0|t0) \left\{ \begin{matrix} l & l' & t \\ L' & L & J \end{matrix} \right\} \left\{ \frac{1}{\xi_e} [(-1)^t W_{t; nL, n'l'}(R, \nu, \xi_e) - W_{t; nL, n'l'}(R, \xi, \xi_e)] - \frac{1}{\nu_e} [(-1)^t W_{t; nL, n'l'}(R, \nu, \nu_e) - W_{t; nL, n'l'}(R, \xi, \nu_e)] \right\} \quad (\text{A16})$$

( $t_{\max}$  is the maximum value of the allowed multipole). Here the next notations are used:

$$W_{t; nL, n'l'}(R, \alpha, \beta) = \mathcal{N}_{nL, n'l'} \sum_{m_1=0}^{n-L-1} S_{m_1}(n, L) \left(\frac{2n'}{n+n'}\right)^{m_1} \sum_{m_2=0}^{n'-l'-1} S_{m_2}(n', L') \left(\frac{2n}{n+n'}\right)^{m_2} \left\{ H_t(x) J_1^{t,s}(x, \lambda_{n, n'}(\alpha, \beta)) - h_t(x) J_2^{t,s}(x, \lambda_{n, n'}(\alpha, \beta)) + F_t(x) J_3^{t,s}(x, \lambda_{n, n'}(\alpha, \beta)) + f_t(x) J_4^{t,s}(x, \lambda_{n, n'}(\alpha, \beta)) \right\}, \quad (\text{A17})$$



where  $x = 2R/\beta$ ,  $s = l + l' + m_1 + m_2$ ,  $\hat{L} \equiv 2L + 1$ ;

$$\mathcal{N}_{nl,n'l'} = \frac{1}{n+n'} \left( \frac{2n'}{n+n'} \right)^{l+1} \left( \frac{2n}{n+n'} \right)^{l'+1} \sqrt{(n+l)!(n-l-1)!(n'+l')!(n'-l'-1)!}; \quad (\text{A18})$$

$$\lambda_{n,n'}(\alpha, \beta) = \frac{2nn'}{n+n'} \frac{a\alpha}{\beta}; \quad (\text{A19})$$

$$H_t(x) = (1 - 2t)h_t(x) + xh_{t+1}(x); \quad (\text{A20})$$

$$F_t(x) = (1 - 2t)f_t(x) - xf_{t+1}(x). \quad (\text{A21})$$

The functions  $h_t(x)$  and  $f_t(x)$  are given by

$$h_t(x) \equiv \sqrt{\frac{2}{\pi x}} K_{t+1/2}(x) \quad (\text{A22})$$

and

$$f_t(x) \equiv \sqrt{\frac{\pi}{2x}} I_{t+1/2}(x). \quad (\text{A23})$$

The radial integrals  $J_i^{t,s}(x, \lambda)$  are defined as follows:

$$J_1^{t,s}(x, \lambda) = \int_0^{x/\lambda} y^{s+2} e^{-y} f_t(\lambda y) dy, \quad (\text{A24})$$

$$J_2^{t,s}(x, \lambda) = \lambda J_1^{t+1,s+1}(x, \lambda), \quad (\text{A25})$$

$$J_3^{t,s}(x, \lambda) = \int_{x/\lambda}^{\infty} y^{s+2} e^{-y} h_t(\lambda y) dy, \quad (\text{A26})$$

$$J_4^{t,s}(x, \lambda) = \lambda J_3^{t+1,s+1}(x, \lambda) \quad (\text{A27})$$

and can be calculated analytically using the power series for the modified Bessel functions or expressed via incomplete gamma functions.

- 
- [1] Th. Strauch et al., Phys. Rev. Lett., **104**, 0142503 (2010).  
[2] M. Bazzi et al., Phys. Lett. **B 704**, 113 (2011).  
[3] D. Gotta et al., Nucl. Phys. **A 660**, 283 (1999).  
[4] M. Leon and H. A. Bethe, Phys. Rev. **127**, 636 (1962).  
[5] E. Borie and M. Leon, Phys. Rev. A **21**, 1460 (1980).  
[6] T. P. Terada and R. S. Hayano, Phys. Rev. C **55**, 73 (1997).  
[7] A. Badertscher et al., Europhys. Lett. **54**, 313 (2001).  
[8] J. F. Crawford et al., Phys. Rev. D **43**, 46 (1991).  
[9] D. J. Abbott et al., Phys. Rev. A **55**, 165 (1997).  
[10] R. Pohl, Ph.D. thesis, ETH Zurich No. 14096, 2001.  
[11] V. E. Markushin, Phys. Rev. A **50**, 1137 (1994).  
[12] T. S. Jensen and V. E. Markushin, Eur. Phys. J. D **21**, 271 (2002).  
[13] D. S. Covita et al., Phys. Rev. Lett., **102**, 023401 (2009).  
[14] D. Gotta et al., Physics of Particles and Nuclei **45**, 181 (2014).  
[15] D. Gotta et al., Hyperf. Interact. **234**, 105 (2015).  
[16] V. P. Popov and V. N. Pomerantsev, Hyperf. Interact. **101/102**, 133 (1996).  
[17] V. P. Popov and V. N. Pomerantsev, Hyperf. Interact. **119**, 133 (1999).  
[18] V. P. Popov and V. N. Pomerantsev, Hyperf. Interact. **119**, 137 (1999).  
[19] V. V. Gusev, V. P. Popov and V. N. Pomerantsev, Hyperf. Interact. **119**, 141 (1999).  
[20] T. S. Jensen and V. E. Markushin, Eur. Phys. J. D **19**, 165 (2002).  
[21] L. Bracci and G. Fiorentini, Nuovo Cimento A **43**, 9 (1978).  
[22] L. I. Ponomarev and E. A. Solov'ev, JETP Lett. **68**, 7 (1998).  
[23] A. V. Kravtsov, A. I. Mikhailov, L. I. Ponomarev, and E. A. Solov'ev, Hyperf. Interact. **138**, 99 (2001).  
[24] T. S. Jensen and V. E. Markushin, Eur. Phys. J. D **21**, 261 (2002).  
[25] L. I. Ponomarev and E. A. Solov'yov, Phys. At. Nucl. **65**, 1575 (2002).  
[26] A. V. Kravtsov and A. I. Mikhailov, Phys. At. Nucl. **69**, 371 (2006).  
[27] M. P. Faifman and L. I. Menshikov, Proc. of Int. Conf. MCF-07, Dubna, p.233 (2007).  
[28] G.Ya. Korenman, V. N. Pomerantsev, and V.P. Popov, JETP Lett. **81**, 543 (2005).  
[29] V. N. Pomerantsev and V. P. Popov, JETP Lett. **83**, 331 (2006).  
[30] V. N. Pomerantsev and V. P. Popov, Phys. Rev. A **73**, 040501(R) (2006).  
[31] V. P. Popov and V. N. Pomerantsev, Phys. Rev. A **83**, 032516 (2011).  
[32] V. P. Popov and V. N. Pomerantsev, Hyperf. Interact. **138**, 109 (2001).  
[33] V. P. Popov and V. N. Pomerantsev, Phys. Rev. A **86**, 052520 (2012).  
[34] V. N. Pomerantsev and V. P. Popov, Hyperf. Interact. **209**, 69 (2012).  
[35] F. F. Karpeshin, Phys. Rev. C **87**, 054319 (2013).  
[36] F. F. Karpeshin and M. B. Trzhaskovskaya, Phys. At. Nucl. **78**, 993 (2015).  
[37] E. Borie, Annals of Physics **327**, 733 (2012); arXiv:1103.1772v7.  
[38] A. Igarashi, I. Shimamura, and T. Shirai, Phys. Rev. A **58**, 1166 (1998).  
[39] Th. Strauch et al., Eur. Phys. J., **A 47**, 88 (2011).  
[40] F. Kottman et al., Hyperf. Interact. **119**, 3 (1999); **138**, 55 (2001).  
[41] R. Pohl et al., Hyperf. Interact. **138**, 35 (2001).  
[42] R. Pohl et al., Phys. Rev. Lett. **97**, 193402 (2006).  
[43] L. Ludhova et al., Phys. Rev. A **75**, 040501(R) (2007).  
[44] R. Pohl et al., Nature (London) **466**, 213 (2010).  
[45] Marc Diepold et al., Phys. Rev. A **88**, 042520 (2013).  
[46] H.-Ch. Schröder et al., Eur. Phys. J. C **21**, 473 (2001).  
[47] D. Gotta, Prog. Part.Nucl.Phys. **52**, 133 (2004).  
[48] D. Gotta et al., Newsletter **15**, 276 (1999).  
[49] D. Gotta et al., Lect. Notes Phys. **745**, 165 (2008).  
[50] D. Gotta et al., Hyperf. Interact. **209**, 57 (2012).  
[51] M. Cargnelli et al., Hyperf. Interact. **209**, 121 (2012).  
[52] T. S. Jensen, V. P. Popov and V. P. Pomerantsev, e-print arXiv:0712.3010.  
[53] V. P. Popov and V. N. Pomerantsev, Hyperf. Interact. **209**, 75 (2012).  
[54] A. V. Kravtsov, A. I. Mikhailov, I. A. Mikhailov and L. I. Ponomarev, Hyperf. Interact. **138**, 103 (2001).  
[55] G. Ya. Korenman and V. P. Popov, Muon Catalyzed Fusion **4**, 145 (1989).  
[56] G. Ya. Korenman, V. P. Popov, and G. A. Fesenko, Muon

- Catalyzed Fusion **7**, 179 (1992).
- [57] J. S. Cohen, Rep. Prog. Phys. **67**, 1769 (2004).
  - [58] H. Anderhub et al., Phys. Lett. B **143**, 65 (1984).
  - [59] N. Bregant et al., Phys. Lett. A **241**, 344 (1998).
  - [60] B. Lauss et al., Phys. Rev. Lett. **80**, 3041 (1998).
  - [61] B. Lauss et al., Phys. Rev. A **60**, 209 (1999).
  - [62] Handbook of Mathematical Functions, edited by M. Abramowitz and I. A. Stegun, National Bureau of Standards, Applied Mathematical Series - 1972.